Three-dimensional modeling of ozone on Mars

Franck Lefèvre,[1] Sébastien Lebonnois,[2] Franck Montmessin,[3] and François Forget[2]

Received 22 March 2004; revised 10 May 2004; accepted 27 May 2004; published 13 July 2004.

[1] We present the first three-dimensional model simulations of ozone on Mars. The model couples a state-of-the-art gas-phase photochemical package to the general circulation model developed at Laboratoire de Météorologie Dynamique (LMD). The results do not contradict the classical picture of a global anticorrelation between the ozone (O_3) and water vapor columns. However, the quantitative approach shows significant departures from this relationship, related to substantial orbital variations in the O_3 vertical distribution. Over the period $L_s = 180°–330°$, low-latitude to midlatitude O_3 is essentially confined below 20 km, has a weak diurnal cycle, and is largely modulated by topography. During the rest of the year ($L_s = 330°–180°$) the model predicts the formation of an O_3 layer at 25–70 km altitude, characterized by nighttime densities about one order of magnitude larger than during the day. Throughout the year, high-latitude O_3 peaks near the surface and reaches maximum integrated amounts ($\sim$40 μm-atm) in the winter polar vortex, with considerable (30 to 50%) dynamically induced day-to-day variations. The most stringent comparison to date with O_3 observational data reveals contrasted results. A good quantitative agreement is found in the postperihelion period ($L_s = 290°–10°$), but the model fails to reproduce O_3 columns as large as those measured near aphelion ($L_s = 61°–67°$). Current uncertainties in absorption cross sections and gas-phase kinetics data do not seem to provide credible explanations to explain this discrepancy, which may suggest the existence of heterogeneous processes. *INDEX TERMS:* 0341 Atmospheric Composition and Structure: Middle atmosphere—constituent transport and chemistry (3334); 5405 Planetology: Solid Surface Planets: Atmospheres—composition and chemistry; 6225 Planetology: Solar System Objects: Mars; *KEYWORDS:* Martian atmosphere, ozone, atmospheric chemistry

Citation: Lefèvre, F., S. Lebonnois, F. Montmessin, and F. Forget (2004), Three-dimensional modeling of ozone on Mars, *J. Geophys. Res.*, *109*, E07004, doi:10.1029/2004JE002268.

1. Introduction

[2] Ozone (O_3) was first observed on Mars by the Mariner 7 and 9 ultraviolet (UV) spectrometers in 1969 and 1971–1972 [*Barth and Hord*, 1971; *Barth et al.*, 1973]. Direct measurements of ozone have then been performed from the Mars 5 and Phobos 2 Russian spacecraft [*Krasnopolsky and Parshev*, 1979; *Blamont and Chassefière*, 1993], from Earth [*Espenak et al.*, 1991], or from the Hubble Space Telescope (HST) [*Clancy et al.*, 1996, 1999]. Since the first modeling studies carried out in the early 1970s [*Parkinson and Hunten*, 1972; *McElroy and Donahue*, 1972], it has been known that the local amount of ozone on Mars is controlled by the abundance in odd hydrogen species (H, OH, HO_2 – HO_x family) produced by the photolysis of water vapor and its reaction with $O(^1D)$. HO_x compounds have also been recognized to be responsible for the apparent stability of the Mars CO_2 atmosphere, by a process that involves the OH-catalyzed recycling of CO into CO_2. Although the more stable hydrogen species H_2O_2 has recently been detected on Mars [*Clancy et al.*, 2004; *Encrenaz et al.*, 2004], HO_x radicals have never been directly measured. Their abundance must be calculated from the amount of water vapor, which has been shown to vary considerably with latitude and season [*Jakosky and Farmer*, 1982; *Smith*, 2002]. This large variability might explain the difficulties encountered by globally averaged chemical models to reach a proper balance between the CO_2 production and loss rates [see, e.g., *Atreya and Gu*, 1994].

[3] Another option is to use ozone, the most active species measured in the Martian atmosphere, as a chemical tracer of the odd hydrogen photochemistry. The abundance of O_3 being so tightly linked to those of HO_x species, the comparison between O_3 measurements and model simulations provides extremely valuable information on our quantitative understanding of the Martian photochemistry. This approach has been used in a number of one-dimensional (1-D) modeling studies [e.g., *Krasnopolsky*, 1993, 2003b; *Nair et al.*, 1994], which showed that a simultaneous agreement between the calculated and observed values of O_3, CO, and O_2 was difficult to achieve when using the standard gas-phase reaction rates. As underlined in these studies, however, one-dimensional models have their own limitations. Although these models are very useful to

[1]Service d'Aéronomie, Institut Pierre-Simon Laplace, Paris, France.
[2]Laboratoire de Météorologie Dynamique, Institut Pierre-Simon Laplace, Paris, France.
[3]Space Science Division, NASA Ames Research Center, Moffett Field, California, USA.

0148-0227/04/2004JE002268$09.00

estimate the globally averaged distribution of chemical species as a function of height, they cannot represent the dramatic latitudinal variations in the distribution of trace species caused by the usually strong pole-to-pole gradient of atmospheric temperature and water vapor. The redistribution of chemical species by horizontal transport is ignored, and a highly uncertain eddy diffusion coefficient has to be used to represent the vertical transport and mixing. The only two-dimensional (2-D) simulation, published by *Moreau et al.* [1991], provided a better description of the interactions between dynamics, radiation, and chemistry, although the model did not include a consistent representation of the water cycle nor a treatment of the dynamics near the surface, where the topographical effects are important. Furthermore, by nature a detailed treatment of the diurnal cycle of chemical species cannot be properly achieved by a 2-D zonally averaged model.

[4] We present here the first general circulation model simulations of the Martian photochemistry. Three-dimensional (3-D) models have a number of advantages over 1-D and 2-D models to represent the chemistry. First, atmospheric transport is fundamentally three-dimensional, and only 3-D models can properly calculate its effects on the distribution of chemical species. Another crucial point is that general circulation models (GCM) are now able to provide a realistic description of the variations in water vapor at all spatial scales and timescales [*Richardson and Wilson*, 2002; F. Montmessin et al., The origin and role of water ice clouds in the Martian water cycle as inferred from a general circulation model, submitted to Journal of Geophysical Research, 2004 (hereinafter referred to as Montmessin et al., submitted manuscript, 2004)]. *Clancy and Nair* [1996] illustrated the necessity of a realistic description of the seasonal water cycle to fully understand the variations in the composition of the Martian atmosphere. Diurnal cycles of temperature and insolation can also be accurately described by GCMs, as well as the effects of topography. All of these factors allow us to make much more stringent comparisons between 3-D model results and coincident measurements.

[5] The aim of this paper is to provide a three-dimensional view of our current understanding of the ozone chemistry on Mars using a state-of-the-art chemical model. We will also compare our results to available O_3 measurements in order to reevaluate our level of quantitative understanding of the Martian photochemistry. Note that we chose to initialize the long-lived species CO, O_2, and H_2 to their observed values and to focus only on the fast photochemistry, after a relatively short (two Martian years) simulation. Therefore the classical problem of the stability of the Mars atmosphere will not be addressed here and will be the subject of a forthcoming study.

2. Model Description

[6] The new chemical model employed in this work is an adaptation of the chemical package used in the Reprobus model developed earlier for the terrestrial stratosphere [*Lefèvre et al.*, 1994, 1998]. It provides a comprehensive description of the oxygen, hydrogen, and CO chemistries on Mars and is implemented as a chemical subroutine into the GCM that has been in development since the early 1990s at Laboratoire de Météorologie Dynamique (LMD). The main characteristics of the chemical routine, the LMD GCM, and the coupling method are described below.

2.1. Absorption Cross Sections and Photolysis

[7] For each photolyzed species we employed the most recent absorption cross sections or the data recommended by *Sander et al.* [2003] commonly used in the modeling of the Earth atmospheric chemistry (Table 1).

[8] For CO_2, shortward of 167 nm, where $O(^1D)$ atoms are produced, cross sections are taken from *Yoshino et al.* [1996a]. At longer wavelengths we used the recent measurements performed at high resolution by *Parkinson et al.* [2003]. The measurements were made at 295 K and 195 K and are available at a wavelength interval of 0.001 nm. At 295 K, data are available up to 200 nm, where a flattening of the measured cross section is noticed. This may indicate the growing relative influence of Rayleigh scattering in this wavelength region, as mentioned by *Shemansky* [1972]. To obtain the CO_2 absorption cross section in this wavelength domain, we subtracted the Rayleigh scattering cross section from the measured cross sections using the expression given by *Atreya and Gu* [1994]. At 195 K, *Parkinson et al.* [2003] data are available only up to 192.5 nm. Beyond this wavelength we extrapolated the cross sections up to 200 nm from the values at 295 K by assuming the same temperature dependence as measured by *Lewis and Carver* [1983] in the 192–197 nm interval. Finally, beyond 200 nm the obtained CO_2 cross sections at 295 K and 195 K were extrapolated by linear decrease with the logarithm of the cross section up to 210 nm. At this wavelength our cross-section value at 195 K (3×10^{-26} cm^2) is identical to the value calculated by *Atreya and Gu* [1994].

[9] Photochemical models of the Mars atmosphere are very sensitive to the values of the absorption cross sections of H_2O, in particular beyond 180 nm, where radiation can penetrate low enough to photolyze the larger water vapor amounts located in the first 30 km above the surface. We use the new laboratory measurements of the H_2O ultraviolet cross sections performed by *Cheng et al.* [1999] over the 140–196 nm spectral range. Data are in relatively good agreement with the cross sections by *Thompson et al.* [1963] generally used in previous studies of the Mars photochemistry but have a largely improved spectral resolution (0.2 nm). H_2O cross sections shortward of 140 nm are from *Yoshino et al.* [1996b].

[10] The UV cross sections for O_2 were taken from *Brasseur and Solomon* [1986] and *Yoshino et al.* [1988] in the Schumann-Runge continuum and Herzberg continuum, respectively. Absorption in the Schumann-Runge bands is explicitly resolved using the temperature-dependent polynomial coefficients determined by *Minschwaner et al.* [1992]. The O_3 cross sections are from *WMO* [1986], also recommended by *Sander et al.* [2003], and include the temperature-dependent measurements of *Molina and Molina* [1986]. HO_2, H_2O_2, and NO_2 cross sections are from *Sander et al.* [2003].

[11] Using the absorption cross sections described above, photolysis rate coefficients (J values) are calculated by the Tropospheric Ultraviolet and Visible (TUV) model [*Madronich and Flocke*, 1998], initially developed to compute the spectral irradiance, actinic flux, and photodis-

Table 1. Photolitic and Chemical Reactions With Their Rate Coefficients and References Used in the Model[a]

	Reaction			Rate Coefficient	Reference
$J_{CO_2-O(1D)}$	$CO_2 + h\nu$	→	$CO + O(^1D)$	0. (at 10 km)	*Yoshino et al.* [1996a]
J_{CO_2-O}	$CO_2 + h\nu$	→	$CO + O$	3.8×10^{-12}	*Parkinson et al.* [2003] *Lewis and Carver* [1983]
$J_{O_2-O(1D)}$	$O_2 + h\nu$	→	$O + O(^1D)$	0. (at 10 km)	*Brasseur and Solomon* [1986]
J_{O_2-O}	$O_2 + h\nu$	→	$O + O$	3.3×10^{-10}	*Minschwaner et al.* [1992] *Yoshino et al.* [1988]
$J_{O_3-O(1D)}$	$O_3 + h\nu$	→	$O_2 + O(^1D)$	3.4×10^{-3}	*Sander et al.* [2003] *Molina and Molina* [1986] *WMO* [1986]
J_{O_3-O}	$O_3 + h\nu$	→	$O_2 + O$	5.6×10^{-4}	*Sander et al.* [2003] *Molina and Molina* [1986] *WMO* [1986]
J_{H_2O}	$H_2O + h\nu$	→	$H_2 + OH$	1.5×10^{-10}	*Cheng et al.* [1999] *Yoshino et al.* [1996b]
$J_{H_2O_2}$	$H_2O_2 + h\nu$	→	$OH + OH$	4.2×10^{-5}	*Sander et al.* [2003] *Schuergers and Welge* [1968]
J_{HO_2}	$HO_2 + h\nu$	→	$OH + O$	2.5×10^{-4}	*Sander et al.* [2003]
J_{NO_2}	$NO_2 + h\nu$	→	$NO + O$	3.9×10^{-3}	*Sander et al.* [2003]
a_{01}	$O + O_2 + CO_2$	→	$O_3 + CO_2$	$1.5 \times 10^{-33}\ (T/300)^{-2.4}$	*Sander et al.* [2003]
a_{02}	$O + O + CO_2$	→	$O_2 + CO_2$	$1.3 \times 10^{-34} e^{900/T}$	*Tsang and Hampson* [1986]
a_{03}	$O + O_3$	→	$O_2 + O_2$	$8.0 \times 10^{-12} e^{-2060/T}$	*Sander et al.* [2003]
b_{01}	$O(^1D) + CO_2$	→	$O + CO_2$	$7.4 \times 10^{-11} e^{120/T}$	*Sander et al.* [2003]
b_{02}	$O(^1D) + H_2O$	→	$OH + OH$	2.2×10^{-10}	*Sander et al.* [2003]
b_{03}	$O(^1D) + H_2$	→	$OH + H$	1.1×10^{-10}	*Sander et al.* [2003]
b_{04}	$O(^1D) + O_2$	→	$O + O_2$	$3.2 \times 10^{-11} e^{70/T}$	*Sander et al.* [2003]
b_{05}	$O(^1D) + O_3$	→	$O_2 + O_2$	1.2×10^{-10}	*Sander et al.* [2003]
b_{06}	$O(^1D) + O_3$	→	$O_2 + O + O$	1.2×10^{-10}	*Sander et al.* [2003]
c_{01}	$HO_2 + O$	→	$OH + O_2$	$3.0 \times 10^{-11} e^{200/T}$	*Sander et al.* [2003]
c_{02}	$OH + O$	→	$H + O_2$	$2.2 \times 10^{-11} e^{120/T}$	*Sander et al.* [2003]
c_{03}	$H + O_3$	→	$OH + O_2$	$1.4 \times 10^{-10} e^{-470/T}$	*Sander et al.* [2003]
c_{04}	$H + HO_2$	→	$OH + OH$	7.3×10^{-11}	*Sander et al.* [2003]
c_{05}	$H + HO_2$	→	$H_2 + O_2$	6.5×10^{-12}	*Sander et al.* [2003]
c_{06}	$H + HO_2$	→	$H_2O + O$	1.6×10^{-12}	*Sander et al.* [2003]
c_{07}	$OH + HO_2$	→	$H_2O + O_2$	$4.8 \times 10^{-11} e^{250/T}$	*Sander et al.* [2003]
c_{08}	$HO_2 + HO_2$	→	$H_2O_2 + O_2$	$1.5 \times 10^{-12} e^{19/T}$	*Christensen et al.* [2002]
c_{09}	$OH + H_2O_2$	→	$H_2O + HO_2$	$2.9 \times 10^{-12} e^{-160/T}$	*Sander et al.* [2003]
c_{10}	$OH + H_2$	→	$H_2O + H$	$5.5 \times 10^{-12} e^{-2000/T}$	*Sander et al.* [2003]
c_{11}	$H + O_2 + CO_2$	→	$HO_2 + CO_2$	$k_0 = 1.4 \times 10^{-31}\ (T/300)^{-1.6}$ $k_\infty = 7.5 \times 10^{-11}$	*Sander et al.* [2003]
c_{12}	$O + H_2O_2$	→	$OH + HO_2$	$1.4 \times 10^{-12} e^{-2000/T}$	*Sander et al.* [2003]
c_{13}	$OH + OH$	→	$H_2O + O$	$4.2 \times 10^{-12} e^{-240/T}$	*Sander et al.* [2003]
c_{14}	$OH + O_3$	→	$HO_2 + O_2$	$1.7 \times 10^{-12} e^{-940/T}$	*Sander et al.* [2003]
c_{15}	$HO_2 + O_3$	→	$OH + O_2 + O_2$	$1.0 \times 10^{-14} e^{-490/T}$	*Sander et al.* [2003]
c_{16}	$HO_2 + HO_2 + CO_2$	→	$H_2O_2 + O_2 + CO_2$	$4.2 \times 10^{-33} e^{1000/T}$	*Sander et al.* [2003]
c_{17}	$OH + OH + CO_2$	→	$H_2O_2 + CO_2$	$k_0 = 1.7 \times 10^{-30}\ (T/300)^{-1.0}$ $k_\infty = 2.6 \times 10^{-11}$	*Sander et al.* [2003]
c_{18}	$H + H + CO_2$	→	$H_2 + CO_2$	$2.2 \times 10^{-32}\ (T/298)^{-0.6}$	*Baulch et al.* [1992]
d_{01}	$NO_2 + O$	→	$NO + O_2$	$5.6 \times 10^{-12} e^{180/T}$	*Sander et al.* [2003]
d_{02}	$NO + O_3$	→	$NO_2 + O_2$	$3.0 \times 10^{-12} e^{-1500/T}$	*Sander et al.* [2003]
d_{03}	$NO + HO_2$	→	$NO_2 + OH$	$3.5 \times 10^{-12} e^{250/T}$	*Sander et al.* [2003]
e_{01}	$CO + OH$	→	$CO_2 + H$	$1.57 \times 10^{-13} + 3.54 \times 10^{-33}[CO_2]$	*McCabe et al.* [2001]
e_{02}	$CO + O + CO_2$	→	$CO_2 + CO_2$	$1.6 \times 10^{-32} e^{-2184/T}$	*Tsang and Hampson* [1986]

[a]Units are s^{-1} for photolysis reactions, $cm^3\ s^{-1}$ for two-body reactions, and $cm^6\ s^{-1}$ for three-body reactions. Photolysis rate coefficients are given at 10 km for the following conditions: solar zenith angle of 60°, sun distance of 1.52 AU, p_{ground} = 6 hPa, midlatitude temperature profile, O_3 column of 1 μm-atm, τ_{dust} = 0.2. Three-body reaction rates have been multiplied by 2.5 to account for the higher efficiency when the third body is CO_2. k_0 and k_∞ are the low- and high-pressure rate coefficients, respectively, for three-body reactions.

sociation in the terrestrial atmosphere. We have adapted TUV to the Martian atmosphere by defining CO_2, O_2, H_2O, and O_3 as the main absorbers of the incident radiation. Solar flux at 1 AU is taken from the high-resolution (0.15 nm) data obtained by the SUSIM instrument [*VanHoosier et al.*, 1988] from 120 to 400 nm and given by *Neckel and Labs* [1984] from 400 to 850 nm. Scattering and absorption through the atmosphere are treated in spherical geometry by the multistream discrete ordinate method of *Stamnes et al.* [1988]. We have adapted the wavelength resolution to describe accurately all of the spectral features in the solar flux or the absorption cross sections: 5 nm in the Chappuis band of O_3, 0.5 nm in the CO_2 band shortward of 175 nm and the Hartley band of O_3, 0.1 nm in the Lyman α region, and 0.01 nm in the CO_2 band longward of 175 nm and in the Schumann-Runge bands of O_2. Temperature dependence of the absorption cross sections is taken into account, as is Rayleigh scattering.

[12] Our calculations also include the absorption and scattering of radiation by dust in the atmosphere. We assumed the vertical optical depth of dust in the UV to be approximately $\tau_{dust} = 0.2$ on a reference pressure level of

6 hPa. Values of up to $\tau_{dust} = 0.3$ are reached in regions of low surface elevation. This is typical of minimum dust-loading conditions, as measured, for instance, by Phobos 2 [*Chassefière et al.*, 1995]. We set the dust UV single-scattering albedo to $\omega = 0.6$ [*Pang and Ajello*, 1977] and set the scattering asymmetry parameter to $g = 0.7$, as in the work of *Krasnopolsky* [1993]. A wavelength-independent value of 0.015 is adopted for the Martian surface albedo, as suggested by the UV observations of *Clancy et al.* [1999].

[13] In order to save computational resources, the photolysis rates are calculated off-line and are stored in a four-dimensional lookup table as a function of the overhead CO_2 column, the overhead O_3 column, the solar zenith angle, and the temperature. The vertical resolution of the table is about 1 km and extends down to a CO_2 column of 3.7×10^{23} cm^{-2} (10 hPa), in order to cover the large surface pressures of the northern hemisphere summer. Different O_3 columns ranging from 0.1 to 50 μm-atm are accounted for in the calculations. Solar zenith angle (SZA) is tabulated from 0 to 95°, with a resolution of 1° beyond 90° to describe the rapidly varying photolysis rates at sunrise and sunset. The temperature dependence of the absorption cross sections is taken into account by using different climatological temperature profiles from the GCM as an input for the photolysis model. Their surface value ranges from 190 K (corresponding to sunlit high latitudes in winter) to 260 K (southern hemisphere summer, noon). The photolysis rates are calculated by TUV and are stored in the table for each of these temperature profiles.

2.2. Gas-Phase Chemistry

[14] In this first study the chemical model computes the three-dimensional distribution of 12 constituents ($O(^1D)$, O, O_2, O_3, H, OH, HO_2, H_2, H_2O, H_2O_2, CO, and CO_2) using the 42 photolytic or chemical reactions listed in Table 1. Most of the rates and branching ratios that we have adopted are those recommended by the Jet Propulsion Laboratory 2003 compilation [*Sander et al.*, 2003]. For reaction c_{08}, we use the rate measured by *Christensen et al.* [2002], which leads to a much better agreement between observed and simulated profiles of H_2O_2 in the terrestrial stratosphere than with the previous recommendations. The rate for the loss mechanism of CO by reaction with OH is from *McCabe et al.* [2001]. As in all of the previous chemical models of the Mars atmosphere, we also increased the rates of the reactions tabulated with N_2, O_3, or Ar as a third body. We chose a factor of 2.5 to account for the greater efficiency of CO_2, identical to the value used by *Nair et al.* [1994].

[15] For long-lived species (O_2, H_2, H_2O, CO) the rate of chemical change is solved using the implicit method described by *Shimazaki* [1985], which we include in an iterative procedure to ensure mass conservation. This technique is also applied to H_2O_2, which has a long lifetime in darkness, and to the chemical families O_x and HO_x, which we define as $O_x = O + O_3$ and $HO_x = H + OH + HO_2$.

[16] During the day the O_x family has a short lifetime in the lower atmosphere (less than half an hour at the hygropause level), and we use a chemical time step of 10 min. Within the O_x and HO_x families, only the members O_3, OH, and HO_2 are assumed to be in photochemical equilibrium. The species O and H, which have a long lifetime at high altitudes, are derived from the concentration of the family and the calculated ratios $\frac{O}{O_3}$, $\frac{H}{HO_2}$, and $\frac{OH}{HO_2}$. $O(^1D)$ is assumed to be in photochemical equilibrium at all heights. At night, photolysis processes vanish, and the hypothesis of photochemical equilibrium does not hold for O_3. In these conditions, O and O_3 are integrated separately, but a short time step of 10 min is conserved to describe properly the fast conversion of O into O_3 at sunset, especially in the lower atmosphere. We also use a simplified treatment of the nitrogen chemistry in order to account for the reaction d_{03} breaking the O-O bond via NO. As pointed out by *Krasnopolsky* [1993], this reaction is an indirect source of O_x and increases the ratio $\frac{OH}{HO_2}$ in the lowermost atmosphere. The $NO_x = NO + NO_2$ mixing ratio is set to 0.6 ppbv, as obtained below 30 km by *Nair et al.* [1994] with their comprehensive model of the nitrogen chemistry. NO and NO_2 are then derived from the justified hypothesis of photochemical equilibrium within the NO_x family.

[17] We consider the results presented in this paper as a baseline case which only takes into account chemical processes that are well identified and supported by reasonably accurate kinetics data. The effects of more speculative processes, such as heterogeneous reactions involving HO_x species on airborne particles or chemical interactions between the atmosphere and the regolith, are, for the present time, ignored in these first simulations.

2.3. Coupling to the LMD General Circulation Model

[18] A recent description of the LMD general circulation model is given by *Forget et al.* [1999]. In the updated version used here, the Martian topography is based on the elevations measured by the Mars Orbiter Laser Altimeter (MOLA) [*Smith et al.*, 1999], and the model is vertically extended up to 120 km altitude using non-LTE radiative transfer calculations [*Angelats-i-Coll et al.*, 2004; F. Forget et al., manuscript in preparation, 2004]. The amount of airborne dust used in the GCM is prescribed and varies with latitude, altitude, and solar longitude. This "dust scenario" was designed by *Forget et al.* [2001] in order to match most of the thermal profiles observed by the Radioscience instrument [*Hinson et al.*, 1999] and the Thermal Emission Spectrometer (TES) [*Smith et al.*, 2001] on board Mars Global Surveyor. For the moment, the evolving dust loading used in the GCM differs from the constant dust amount considered in the photochemical module, but both data sets will be unified in the next version of the coupled model. Note that the effect of a varying dust opacity on photolysis rates and ozone is later examined in the present work.

[19] The GCM incorporates a comprehensive physical modeling of the Martian water cycle using a microphysical scheme to describe the sublimation and condensation processes as well as the sedimentation of water ice particles in the atmosphere. This new version of the GCM water cycle is described in detail by Montmessin et al. (submitted manuscript, 2004). Water ice particles are transported by the model winds, as is water vapor and all of the chemical species. Transport of tracers is calculated using a second-order finite volume scheme with slope limitation [*Van Leer*, 1977; *Hourdin and Armengaud*, 1999]. Turbulent mixing of chemical species at the subgrid-scale is also taken into account from the turbulent kinetic energy diagnosed by the model in each grid box (see *Forget et al.* [1999, and references therein] for a complete description of the

scheme). In addition, a standard energy-conserving convective adjustment scheme rapidly mixes heat, momentum, and tracers in convectively unstable layers.

[20] At each model time step the CO_2, H_2O, and other chemical fields are exchanged between the GCM and the chemical routine to achieve a fully interactive coupling between dynamics, radiation, water cycle, and chemistry: every 10 min the photochemical routine is called to calculate the atmospheric chemical composition in all GCM grid cells. Chemical reaction rates are calculated using the GCM temperature and pressure profiles. For the photodissociation rates, the CO_2 and O_3 vertical columns are first computed for all the grid points located in sunlight. The actual J values used in the chemistry are then interpolated in CO_2, O_3, and SZA within the lookup table. Finally, the photolysis rates obtained at 1.52 AU are scaled to their appropriate value according to the exact Sun-Mars distance calculated by the GCM. The ~40% variation in solar flux during the Martian year, which results from the large eccentricity of the Mars orbit, is therefore taken into account in our simulations.

[21] The condensation of hydrogen peroxide (H_2O_2) is also taken into account by means of a simplified scheme that compares the H_2O_2 pressure to its vapor pressure at saturation [*Lindner*, 1988] and transfers the excess quantity to the level below. If saturation occurs near the ground, H_2O_2 is deposited on the surface as H_2O_2 ice. For the moment, sublimation of this surface deposit is not implemented in the model.

[22] The coupled model was run on 32 vertical levels with a horizontal resolution of 64 longitudes by 48 latitudes (5.625° × 3.75°). The initial state includes a water cycle fully established after appropriate spin-up time and uniform mixing ratios for the well-mixed species O_2 (1.3×10^{-3} [*Owen et al.*, 1997]), CO (8×10^{-4} [*Lellouch et al.*, 1991; *Krasnopolsky*, 2003a]), and H_2 (1.5×10^{-5} [*Krasnopolsky and Feldman*, 2001]). The results presented here were obtained after two Martian years of simulation.

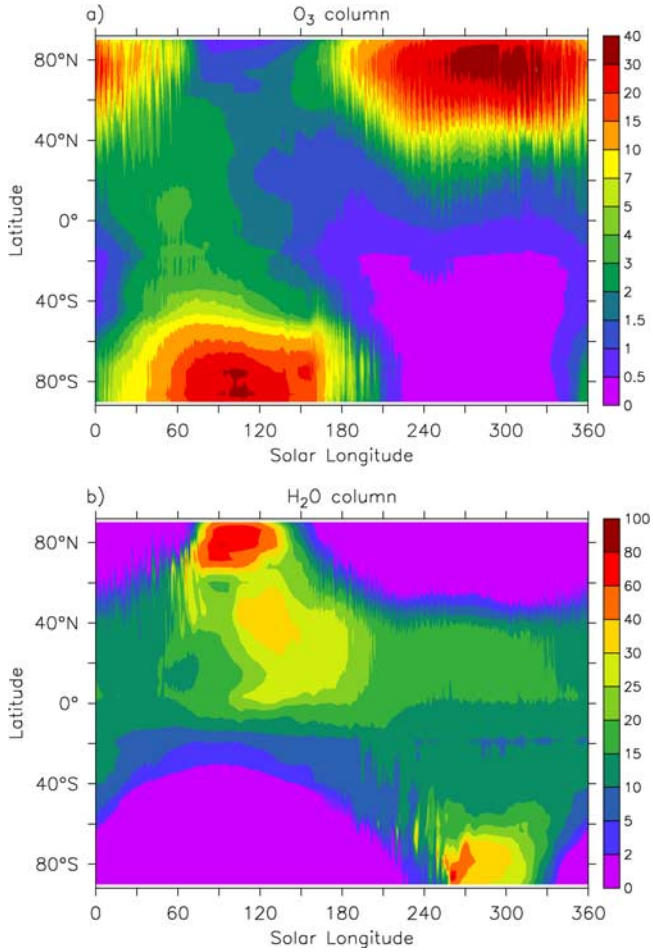

Figure 1. (a) Zonally averaged ozone column (μm-atm) and (b) zonally averaged water vapor column (precipitable microns, pr-μm) as a function of solar longitude.

3. Results

3.1. Ozone Total Column

[23] Ozone is produced by the photolysis of CO_2 and O_2, followed by the recombination of the product O with O_2. It is destroyed by odd hydrogen catalytic cycles that effectively control the local amount of ozone on Mars. An anticorrelation between the abundances of water vapor, which is the source of HO_x, and ozone is therefore expected in the Martian atmosphere.

[24] The overall behavior of the ozone seasonal evolution calculated by the model may be examined in Figure 1, showing the zonally averaged ozone column as a function of latitude and solar longitude (L_s). Note that the values are here averaged over 24 hours and are therefore a mean of daytime and nighttime abundances. Compared to Earth, the extremely strong spatial and temporal variations in ozone are a striking feature of the Martian atmosphere: there is a factor of about 100 between the largest ozone columns, calculated at high latitudes in winter, and the smallest amounts, obtained in the southern hemisphere around perihelion and summer solstice. The O_3 column evolution can be related to the water vapor abundance calculated by the model, also shown in Figure 1. A detailed discussion of the results regarding the water cycle in the LMD GCM is given by Montmessin et al. (submitted manuscript, 2004), who note a good quantitative agreement with the measurements of the water vapor column performed by TES on board Mars Global Surveyor [*Smith*, 2002]. At first glance the anticorrelation between the ozone and water vapor columns seems clearly visible. At high latitudes of both hemispheres the ozone column is maximum in winter, when condensation on polar caps suppresses most of the atmospheric water vapor. Polar ozone is minimum in summer, indicating an efficient O_3 destruction by the HO_x radicals released from the large amounts of water vapor and sunlight. However, the O_3 polar minimum also presents a strong north/south asymmetry: the ozone abundance at high latitudes in southern summer is smaller than that in northern summer by a factor of 4 (~0.5 μm-atm and ~2 μm-atm, respectively), despite a smaller water vapor abundance in southern summer. This departure from the O_3-H_2O anticorrelation is related to differences in the H_2O vertical distribution. The same reason explains the O_3 column orbital cycle in the equatorial region, where there is about three times more ozone shortly before aphelion (~3 μm-atm at $L_s = 60°$) than at perihelion (~1 μm-atm at $L_s = 250°$), although the water column amount is similar in both cases (15 pr-μm).

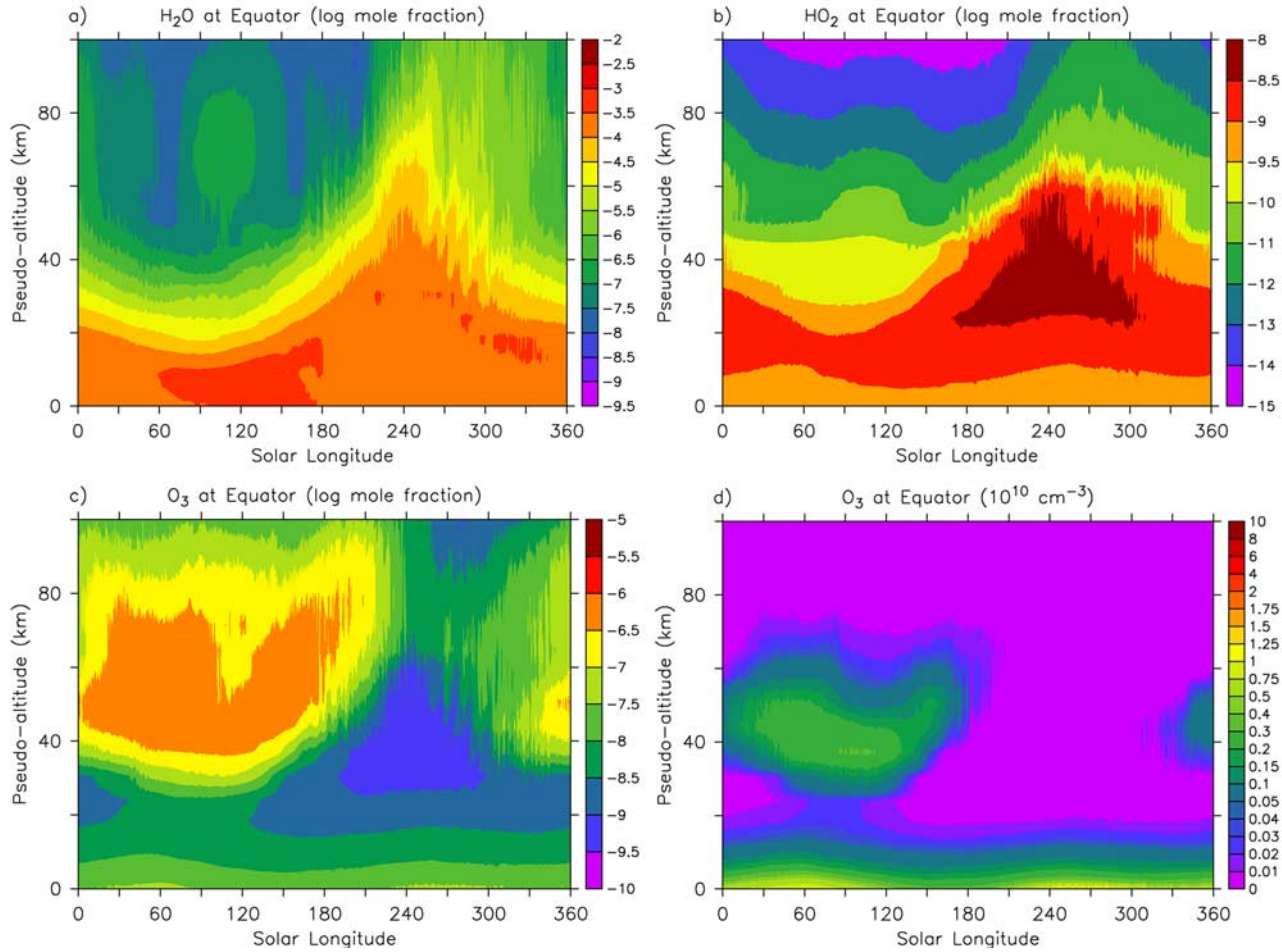

Figure 2. Zonally averaged vertical profiles at the equator as a function of solar longitude. (a) H_2O mixing ratio, (b) HO_2 mixing ratio, and (c) O_3 mixing ratio, all in log scale. (d) O_3 number density ($\times 10^{10}$ cm^{-3}). Pseudoaltitude is calculated from the terrain-following σ coordinate system (σ is pressure divided by surface pressure) using a constant scale height $H = 10$ km. Difference with altitude is less than 1 km up to ∼30 km, ∼5 km at 60 km, and ∼15 km at 100 km.

[25] Thus it appears that the picture of a global O_3-H_2O anticorrelation is strictly verified only for a given solar longitude. When considering a single latitude band over the Martian year, the O_3 column may show little correlation with the H_2O column, especially at low latitudes. The sign of the correlation may even reverse and become positive if one compares the O_3 and H_2O columns for the same season of different hemispheres (i.e., the northern and southern polar winters). These differences in the O_3-H_2O relationship are related to variations with L_s in the altitude of water vapor saturation, which will be discussed in the next sections. They must be kept in mind when analyzing measurements of the vertically integrated amounts of O_3 and H_2O taken at different times (L_s) of the Martian year.

3.2. Ozone Vertical Distribution

[26] The photochemical theory predicts substantial changes in the vertical distribution of low-latitude to mid-latitude ozone on Mars. Using a one-dimensional model forced by a simple stepwise annual cycle of the water vapor profile, *Clancy and Nair* [1996] showed that the ozone variations above 10 km were essentially driven by the annual cycle of the hygropause altitude. This process is confirmed by our three-dimensional simulation, which predicts a smoothly varying evolution of the water vapor vertical distribution during the Martian year. Figure 2 shows the annual cycles of the diurnally averaged H_2O and O_3 profiles calculated by the model at the equator as a function of solar longitude. Above 20 km the H_2O vertical distribution is clearly determined by the variations in temperature, in response to the evolution of dust and solar flux along the Mars orbit. Around aphelion ($L_s = 60°–120°$) the cold and dust-free atmosphere leads to a low saturation altitude for water vapor (10–15 km), with rapidly decreasing mixing ratios above the hygropause. Immediately after aphelion the water saturation altitude shows a steady increase until $L_s = 250°$ at perihelion. In the warmer and dustier conditions of this time of the year, water vapor saturation occurs in the model above 40 km altitude. We note that the seasonal evolution of the water condensation level calculated by the model at the equator is in excellent agreement with the TES observations [*Smith*, 2002]. The ∼30 km rise of

the hygropause that occurs from perihelion to aphelion causes very large annual variations of the water content above 20 km, with a difference of two to three orders of magnitude at the equator between the two extreme points of the orbit. In the sunlit conditions of low latitudes to midlatitudes this substantial change has strong implications on the amount of odd hydrogen produced by the photolysis of H_2O. HO_2 is an indirect product of the H_2O photolysis. As shown in Figure 2, the HO_2 vertical distribution is closely correlated to H_2O in the lower atmosphere. The largest HO_2 abundance (several ppbv) calculated by the model occurs around perihelion in an altitude layer between 20 and 50 km. This is where the product of the water vapor concentration and its photolysis rate J_{H_2O}, related to the intensity of the UV flux, reaches its maximum value. There is also some indication of cross-hygropause transport of HO_2 at $L_s = 270°–320°$. The photochemical lifetime of the HO_x family is indeed of the order of a few days at 40–50 km. In the case of ascending motions near the hygropause level the upward transport of increased HO_x coming from the lower atmosphere may affect the photochemistry at levels located above the H_2O saturation altitude.

[27] In Figure 2 the ozone profile at the equator responds quickly to the annual variations in HO_x. From $L_s = 0°$ to $L_s = 180°$ the 24 hour averaged ozone mixing ratio shows a layer of a few tenths of ppmv between 40 km and 80 km, well anticorrelated with the H_2O abundance calculated during this cold and dry period. Starting at $L_s = 150°$ and as Mars approaches its perihelion, more water vapor is allowed to reach high altitudes. A gradual decrease in ozone is clearly visible and propagates upward until $L_s = 250°$, when the hygropause reaches its highest level. During this period the massive release of odd hydrogen species leads to a dramatic ozone loss between 30 and 80 km altitude. The ozone layer that was present in this altitude range almost entirely disappears and is replaced by an absolute O_3 minimum, with mixing ratios lower by three orders of magnitude compared to the aphelion season. Results plotted in terms of number density reveal, in daily average, two distinct altitude regions:

[28] 1. Below 20 km the O_3 "surface layer" shows a weak annual cycle that slowly evolves as a function of the available water vapor and the heliocentric distance. The maximum thickness of this layer is computed shortly before aphelion ($L_s = 60°$) and at perihelion ($L_s = 250°$). Near the equator this is when the product of the low atmosphere H_2O density and the solar flux intensity is minimum. Interestingly, the stronger solar flux at perihelion is compensated by a decreased near-surface H_2O, resulting in similar O_3 amounts for both periods.

[29] 2. Above 20 km the O_3 "aphelion layer" extends up to ~70 km but exists for only about half of the Martian orbit ($L_s = 330°–180°$), centered on aphelion. This layer disappears almost entirely for the rest of the year. The orbital variability of the layer, where the peak densities are comparable to those calculated in the first 10 km above the surface, is clearly responsible for the factor of ~3 increase in the O_3 column that is simulated at low latitudes from the perihelion to the aphelion season (Figure 1).

[30] This process also explains the differences between our results and those calculated by the two-dimensional chemical model of *Moreau et al.* [1991], who found almost no variability with L_s in the low-latitude O_3 column. In their simulation, *Moreau et al.* [1991] used prescribed water vapor fields designed to reproduce the Viking measurements [*Jakosky and Farmer*, 1982], assuming a H_2O vertical decrease with a fixed scale height over the Martian year. Clearly, this assumption does not hold during the whole annual cycle, and it is likely that the amplitude of the variation in the H_2O saturation altitude was underestimated. This emphasizes the advantage of the interactive coupling between the chemistry and a physically based water cycle for more accurate simulations of ozone on Mars, under the necessary condition that the H_2O amounts calculated by the model are in good quantitative agreement with the observations.

[31] The ozone annual cycle obtained in both layers defined above compares favorably with the ozone profiles calculated at $L_s = 60°$ and $L_s = 240°$ by *Clancy and Nair* [1996]. As seen in Figure 2d, the peak O_3 density computed in the middle atmosphere layer near aphelion is about 0.4×10^{10} cm^{-3}, which is in rather good agreement with their 1-D study. The altitude of the peak is higher by about 20 km in our simulation. This results from the higher hygropause and weaker H_2O vertical gradient above the saturation altitude in the 3-D model. In terms of the O_3 vertical column the factor of ~3 increase that we obtain at low latitudes from perihelion to aphelion is in excellent agreement with *Clancy and Nair* [1996].

3.3. Ozone Diurnal Cycle

[32] Previous one-dimensional modeling studies have shown that ozone may be highly variable during the Martian day [*Krastitsky*, 1978; *Shimazaki*, 1981; *Nair et al.*, 1994]. In our model the O_3 column is on average larger during nighttime than during the day. However, the amplitude of this diurnal cycle varies largely with latitude and solar longitude. To illustrate this, Figure 3 displays the instantaneous total O_3 field calculated by the model in four Martian seasons, with local noon at longitude 0. At northern spring equinox ($L_s = 0°$), no O_3 diurnal cycle is apparent at high latitudes, whereas the sunlit part of the 40°N–40°S latitude band is characterized by significantly lower O_3 values. In this region the O_3 columns calculated in daylight are about four times smaller (~0.5 μm-atm versus ~2 μm-atm) than those obtained at night. The O_3 column distribution also shows a substantial modulation by topography: large O_3 columns are calculated in sunlight from the Chryse Planitia low plain to Valles Marineris, whereas strong O_3 reductions are associated with elevated regions such as the Tharsis Ridge and Alba Patera. This indicates a major contribution to the column of the O_3 surface layer. Although there is some indication of a late morning secondary maximum of photochemical origin at 30°S, the variations in the O_3 sunlit distribution are dominated, at this season, by the topography. During the night, no significant O_3 variation with local time is apparent. The synoptic map for northern summer ($L_s = 90°$) shows globally larger ozone columns, with a factor of about two between the nighttime values (~4 μm-atm) and the more apparent late morning maximum (~2μm-atm). Slightly smaller O_3 columns are calculated at sunrise and in the late afternoon. The topographic structures are also less visible in the O_3 field. Only Alba Patera appears at sunrise as a ~50% decrease in the O_3 column, as well as the Hellas

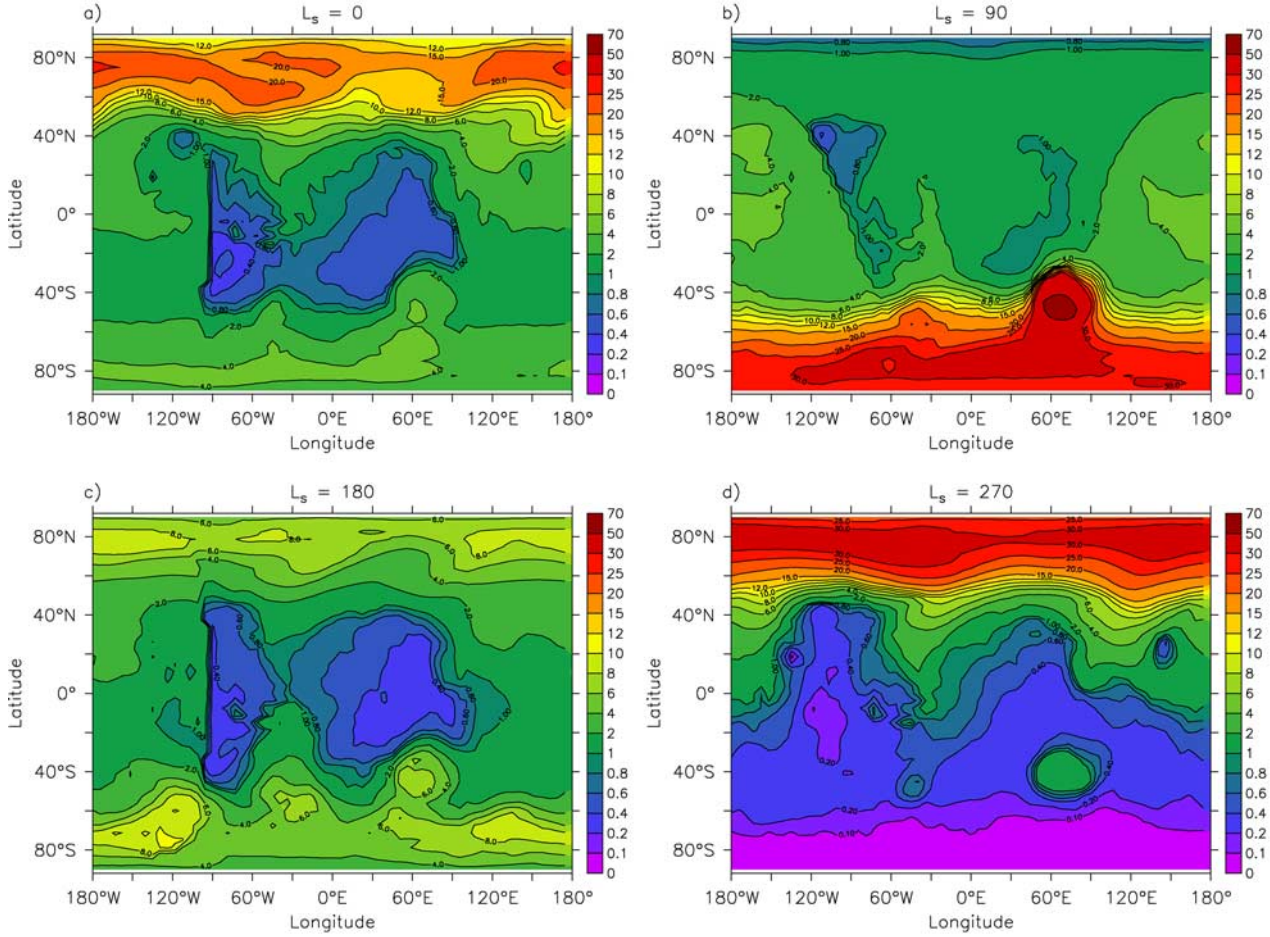

Figure 3. Instantaneous distribution of the ozone column (μm-atm) at four seasons. Local noon is at longitude = 0. (a) $L_s = 0°$, (b) $L_s = 90°$, (c) $L_s = 180°$, and (d) $L_s = 270°$.

basin, where the extreme surface pressure favors the accumulation of O_3 near the ground. Maximum O_3 amounts fill the entire polar night region. The northern fall equinox (L_s = 180°) O_3 distribution is similar to what is obtained for spring. Again, the daytime O_3 column is far from being uniformly distributed owing to variations in surface elevation. Finally, the results for northern winter (L_s = 270°) show much less ozone than for all other seasons at all latitudes southward of 40°N. No diurnal cycle is seen, and the O_3 column distribution reflects entirely the variations in topography, suggesting a maximum contribution of the O_3 surface layer to the total column. As in southern winter, the largest O_3 amounts are computed in the polar night region, with a rather homogeneous distribution.

[33] An example of the diurnal variation of ozone along the vertical is given in Figure 4, showing the variation with local time of the O_3 profile at the equator, for four different seasons. As already seen in Figure 2, during the first two seasons ($L_s = 0°–30°$ and $L_s = 60°–90°$) the ozone density profile is characterized by a double-layer structure, peaking near the ground for the surface layer below 20 km and located between 25 and 70 km at night in the middle atmosphere layer. The middle atmosphere O_3 layer is maximum in the aphelion season, is vanishing at the northern fall equinox, and has totally disappeared by the perihelion season. In terms of diurnal variation the surface and altitude O_3 layers exhibit very different behavior:

[34] 1. Below 20 km the available amount of O is small, and the nighttime conversion of O to O_3 does not lead to a large variation with local time. In the model the largest daytime O_3 variation is actually found in the first ~3 km above the Martian surface. At these levels a considerable increase in temperature (+60 K) may occur between sunrise and afternoon. At sunrise the low atmospheric temperatures favor reaction d_{03}, converting NO into NO_2. Subsequent photolysis of NO_2 produces O atoms and an early morning O_3 peak. Then, the rapid warming of the atmosphere slows down the reaction a_{01}, producing ozone, and may even inhibit the formation of the noon O_3 maximum that is calculated at higher levels in the model. The combination of both effects leads to a daytime maximum occurring at about 1000 LT, when the O_3 column is vertically integrated. At night, O_3 is affected only by the slow reaction c_{15} and can be considered as a quasi-passive tracer in the whole 0–20 km layer.

[35] 2. Above 20 km the amount of O rapidly increases with altitude. The fast conversion between O and O_3 induces a significant diurnal cycle in the O_3 layer that forms in the middle atmosphere between $L_s = 0°$ and $L_s = 180°$. During this period the nighttime O_3 number density is

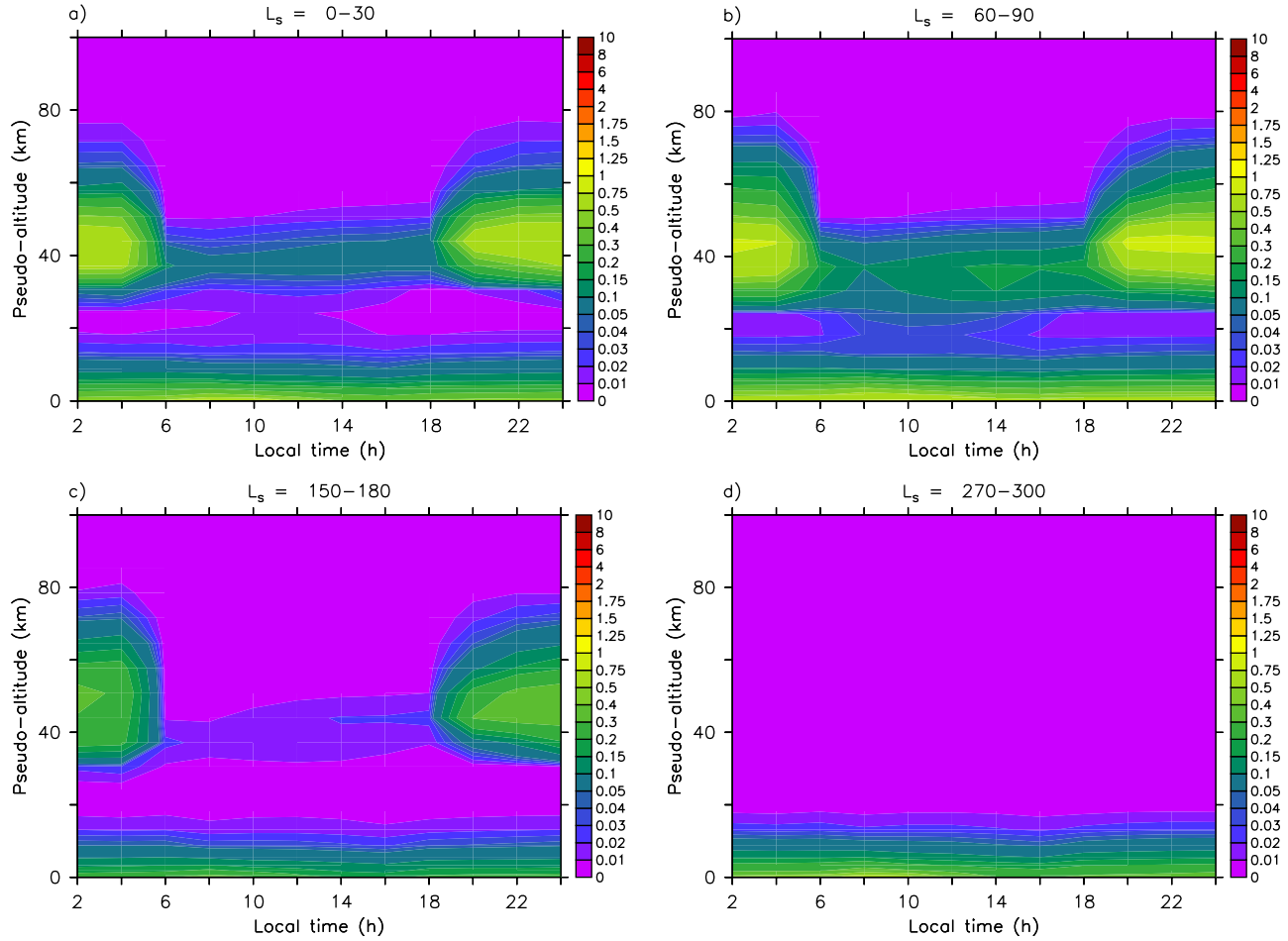

Figure 4. Diurnal variation of the vertical profile of ozone density ($\times 10^{10}$ cm^{-3}), at the equator and longitude = 0°, averaged over four different seasons: (a) L_s = 0°–30°, (b) L_s = 60°–90°, (c) L_s = 150°–180°, and (d) L_s = 270°–300°.

comparable to what is obtained near the surface but is about one order of magnitude smaller during the day ($\sim$0.1 $\times$ 10^{10} cm^{-3} versus $\sim$1 $\times$ 10^{10} cm^{-3}). Most of the diurnal variation observed in the total O_3 column can therefore be attributed to the O_3 diurnal variation in the middle atmosphere, since the thickness of the O_3 surface layer does not undergo much change during the Martian day. As seen earlier, the O_3 layer at 25–70 km also shows considerable variations with L_s, and this is the main cause for the seasonal change in the O_3 column diurnal cycle: at the equinoxes the amplitude of the diurnal cycle in the middle atmosphere is maximum, leading to a substantial difference between the daytime and nighttime O_3 columns (Figures 3a and 3c). In contrast the absence of any apparent diurnal cycle in the total O_3 field calculated near perihelion (Figure 3d) is a direct consequence of the disappearance of the O_3 middle atmosphere layer.

3.4. Ozone at Polar Latitudes

[36] The maximum abundances of O_3 are observed at polar latitudes, where O_3 also exhibits the greatest seasonal variability. The O_3 behavior predicted by our model in these regions is discussed here more specifically.

[37] Figure 5 displays the calculated seasonal cycle of the ozone column zonally averaged at 70°N and 70°S. The overall seasonal evolution is similar in the two hemispheres. It can be described by a O_3 minimum in summer, a rapid buildup after fall equinox, maximum values in winter, and a decline in spring. In the southern hemisphere the O_3 column at 70°S is greatest at winter solstice (L_s = 90°) and reaches a maximum value of 27 μm-atm. In the northern hemisphere, O_3 continues to increase after solstice to reach maximum values approaching 40 μm-atm at L_s = 320°. This mean behavior is accompanied by variations at short timescales that are particularly apparent during the northern hemisphere winter and spring. According to the model, the late winter O_3 at 70°N can easily vary by ±10 μm-atm (i.e., 30 to 50%) in a 24 hour interval. Figure 6 illustrates the origin of this variability. The synoptic maps of the O_3 column plotted at 12 hour intervals from L_s = 350° to L_s = 353° exhibit a strong O_3 maximum confined inside the polar vortex, with maximum values of about 40 μm-atm. At this time of the year the ozone column has already started to decrease at 70°N (Figure 5) but shows a maximum variability. A striking feature of the O_3 geographical distribution is the considerable day-to-day changes associated with the dynamical disturbances of the polar vortex. Baroclinic waves have a maximum activity in late winter and spring. This results in rapidly evolving distortions of the polar vortex edge that are easily identifiable by the steep O_3

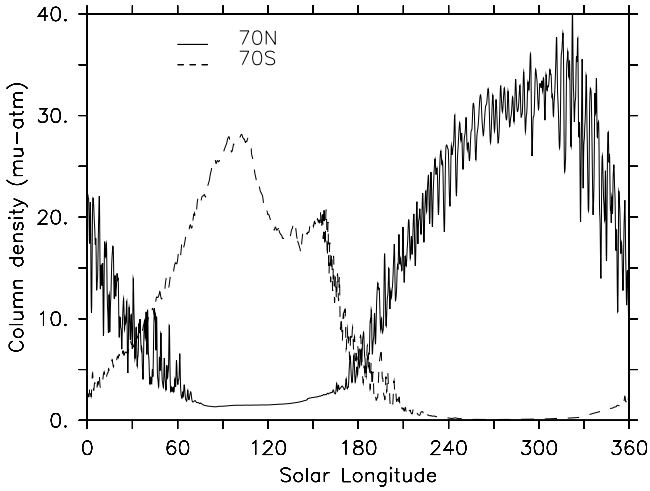

Figure 5. Ozone column (μm-atm) as a function of solar longitude, zonally averaged at 70°N (solid) and 70°S (dashed).

gradients. Note that although solar light has almost reached the pole at this time of the year, there is no apparent diurnal cycle in the O_3 column field. Wintertime polar O_3 is indeed essentially confined near the surface (Figure 7), where the concentration of O atoms is low and does not induce O_3 variations at sunrise and sunset. Furthermore, at $L_s \simeq 350°$ the HO_x production at 70°N is virtually zero: as shown in Figures 1 and 7a, the cold polar vortex remains isolated from the midlatitude air and is still extremely dry. Less than 1 pr-μm total H_2O is computed by the model, with only ~1 ppmv at the surface. Note that the short duration of the day and the large SZAs do not allow significant H_2O photolysis anyway. In these conditions, HO_x may be produced in the model by reaction b_{03}:

$$O(^1D) + H_2 \rightarrow OH + H$$

However, $O(^1D)$ is produced by O_3 photodissociation, which is itself attenuated by the significant O_3 opacity. In accordance with *Lindner* [1988], dust also contributes to reduce largely the O_3 photolysis at large SZA, even in the relatively clean conditions assumed in the model (τ_{dust} = 0.2). Thus O_3 can be considered as a quasi-passive tracer inside the polar vortex at least until spring equinox. Its variations over short timescales at latitudes close to the vortex edge may be entirely attributed to variations in the shape of the polar vortex.

[38] Although similar in character, the behavior of polar ozone also shows some asymmetry between the northern and southern hemispheres. In winter the day-to-day variability is much less at 70°S than at 70°N. This can be attributed to the weaker wave activity of the southern high latitudes. Ozone is a good tracer of dynamics at this time of the year, and from Figure 1 it is evident that the vortex edge has a smooth evolution in latitude and is little perturbed until $L_s \simeq 150°$. In summer, polar ozone is close to zero in the southern hemisphere, whereas amounts of 1.5 μm-atm are computed in the northern hemisphere. This difference is again linked to the vertical distribution of water vapor and is clearly illustrated in Figure 7. At 70°N the low atmospheric temperatures that prevail near aphelion prevent H_2O from reaching high altitudes: even at solstice (L_s = 90°) the H_2O mixing ratio decreases rapidly with height, and the 100 ppmv contour remains confined below 30 km. In stark contrast, the H_2O vertical distribution at southern hemisphere solstice (L_s = 270°) shows a dramatic vertical expansion, bringing the 100 ppmv contour up to 90 km altitude. To this large increase in the H_2O amount must be added the effect of the ~40% faster photolysis at perihelion compared to aphelion. The consequence on low-atmosphere O_3 is a mixing ratio about one order of magnitude smaller in southern summer than in northern summer. Thus the north-south asymmetry in summertime O_3 at high latitudes is essentially of photochemical origin, the differences in topography playing only a marginal role at this season.

[39] The diurnal cycle of the ozone vertical profile at 70°N (Figure 8) does not show, in general, a double-layer structure comparable to what is found at the equator. The main cause for this difference is the much drier environment that characterizes the northern polar region for most of the year. Large SZAs also contribute to slowing down the production of HO_x from H_2O photolysis. In these conditions the maximum O_x loss that usually occurs in the 10 km layer below the hygropause is largely inhibited, and O_3 decreases monotonically with height up to 40 km. It is only in the aphelion season (L_s = 60°–90°) at 70°N that an O_3 minimum is apparent at 20–30 km. H_2O abundance is maximum at this time of the year, resulting in an O_3 chemistry comparable to that of low latitudes to midlatitudes. In other seasons the polar chemistry is much less active, as shown by the reduced O_3 diurnal variation at the equinoxes compared to what is computed at the equator. Another outstanding feature is the large ozone concentration that we obtain throughout the year at the surface level. This is particularly true in the polar night (L_s = 270°–300°), with a O_3 density close to 10×10^{10} cm^{-3} but also in summer (L_s = 60°–90°), though H_2O near the ground is more abundant at 70°N than at the equator. The difference lies in the lower surface elevation of the northern polar region compared to the tropics: in the low plains the stronger UV optical thickness and dust opacity reduce the H_2O and O_3 photolysis rates, whereas the large surface pressure favors the three-body reaction producing O_3.

3.5. Comparison to Observations

[40] The model results are now compared to published observations of the latitudinal distribution of the ozone column on Mars. Unfortunately, these are available only for a limited range of solar longitudes. In the following, NH and SH are used for northern hemisphere and southern hemisphere, respectively.

3.5.1. NH Winter/SH Summer (L_s = 270°–360°)

[41] The first systematic measurements of ozone on Mars were made by the Mariner 9 ultraviolet spectrometer [*Barth et al.*, 1973]. At L_s = 292°–300° the O_3 content above the south polar cap was below the detection limit of the instrument, 3 μm-atm. In January 2002, *Novak et al.* [2003] measured the $O_2(a^1\Delta_g)$ dayglow emission to retrieve the ozone column above ~20 km at about the same season (L_s = 306°). They did not find any ozone in the 30°N–90°S

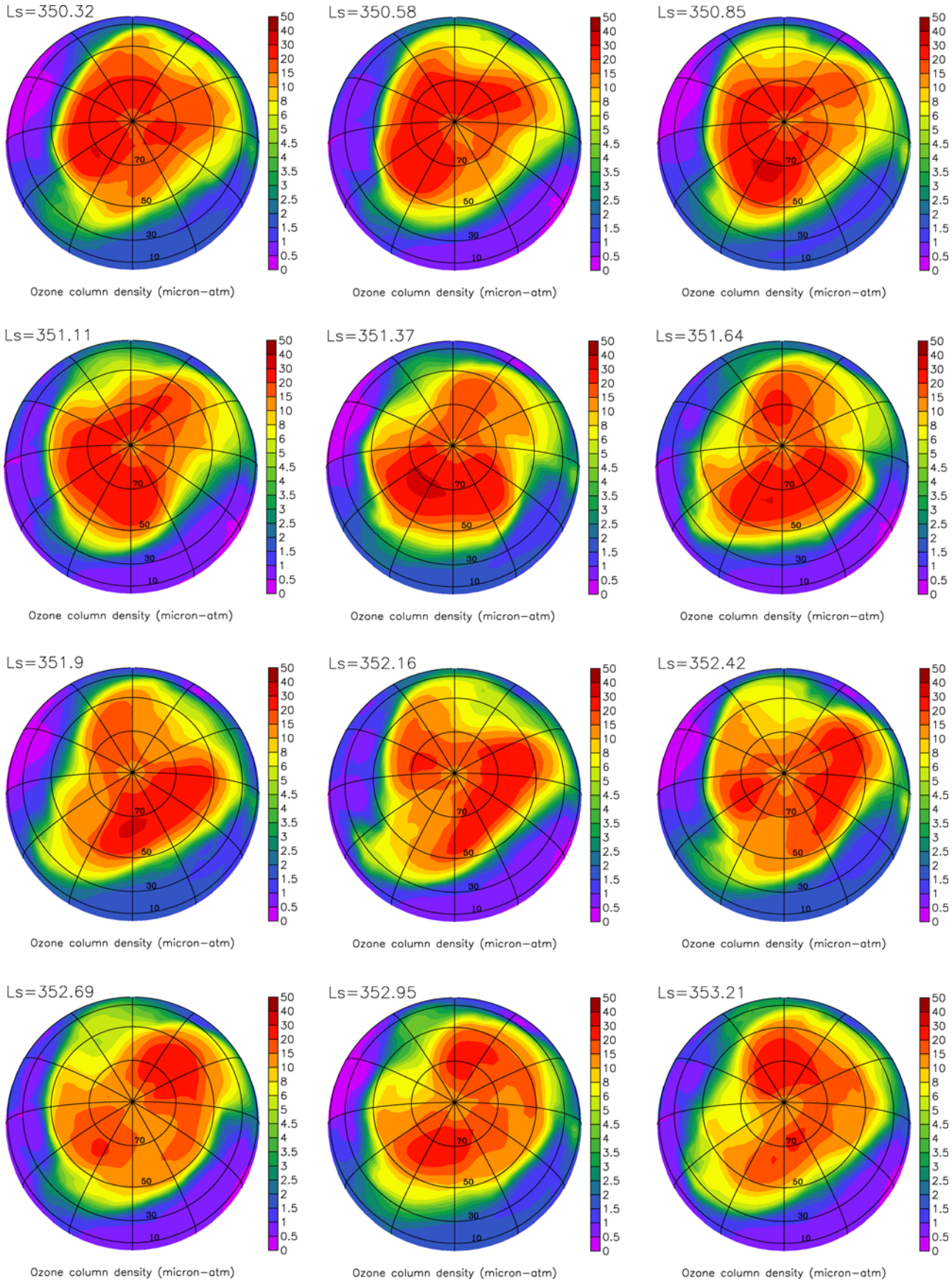

Figure 6. North polar orthographic projections of the ozone column (μm-atm) plotted at 12 hour intervals from L_s = 350° to L_s = 353°.

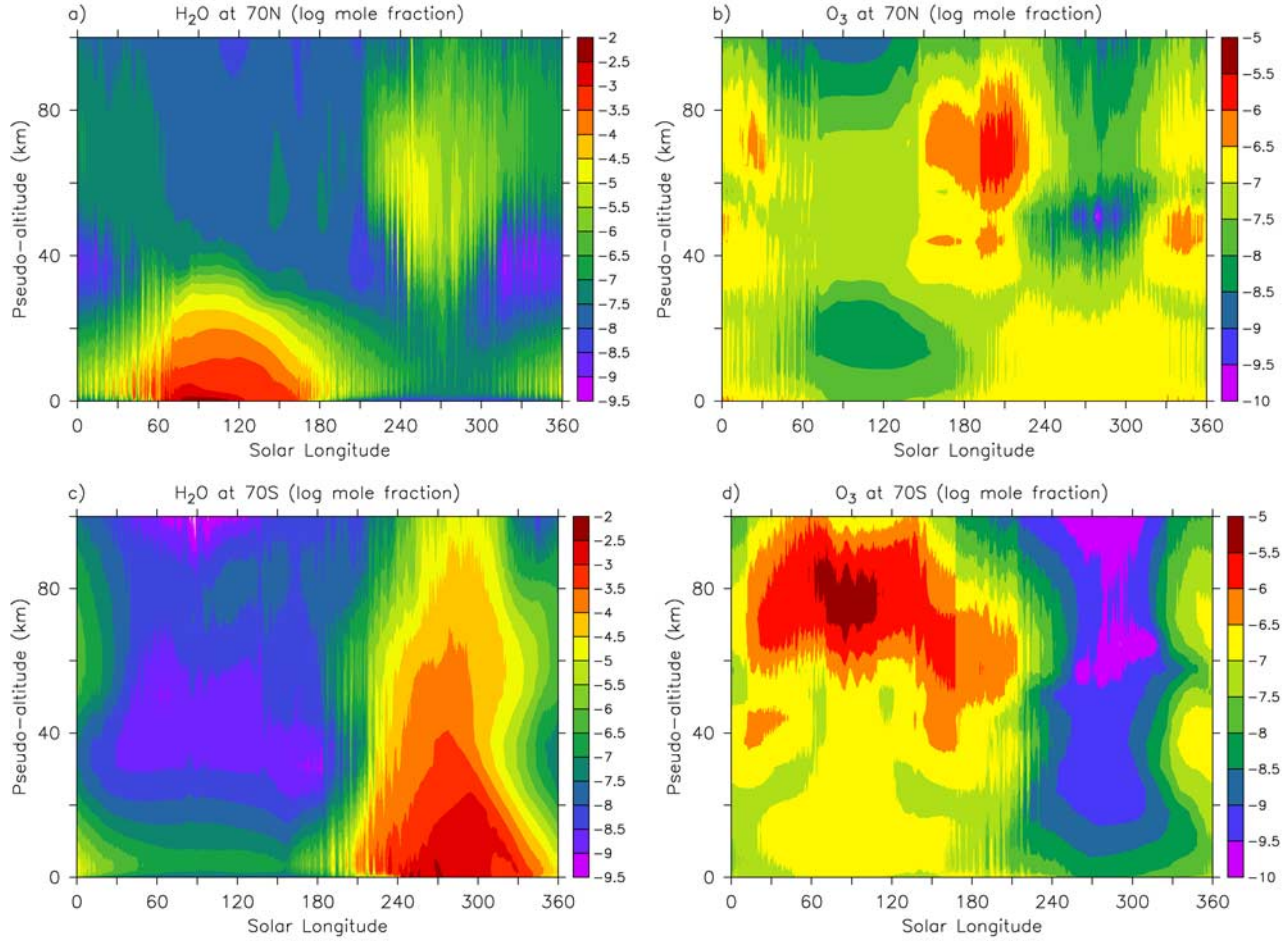

Figure 7. Zonally averaged vertical profiles at high latitudes. (a) H_2O at 70°N, (b) O_3 at 70°N, (c) H_2O at 70°S, and (d) O_3 at 70°S, all expressed as mixing ratio (log scale), as a function of solar longitude.

latitude band above the noise level of 0.1 μm-atm. The model results are consistent with these observations. In Figure 1 the modeled O_3 total column is lower than 0.5 μm-atm over a wide latitude band in SH summer and is indeed well below the detection limit of Mariner 9. In Figure 4d the complete absence of ozone above 20 km in our model also explains the absence of $O_2(a^1\Delta_g)$ emission noted by *Novak et al.* [2003]. At the end of SH summer the maximum O_3 amounts measured by Mariner 9 in the 50°S–75°S latitude band passed above the detection limit at L_s = 330° and reached an amount greater than 10 μm-atm at L_s = 360°. This rapid increase occurs later and is not strong enough in the model. However, measurements of the $O_2(a^1\Delta_g)$ dayglow emission made in January 2004 at L_s = 333° showed no ozone above ~20 km (R. Novak, personal communication, 2004), suggesting a possible interannual variability in the onset of the late summer O_3 increase in the southern hemisphere.

[42] In the northern hemisphere the wintertime (L_s = 330°–360°) measurements by Mariner 9 revealed the largest O_3 amounts ever observed on Mars. Values up to 60 μm-atm were detected in the 50°N–75°N latitude band [*Wherbein et al.*, 1979] but also showed wide variations from day to day. From the Mariner 9 individual observations presented by *Traub et al.* [1979] it appears that the O_3 amounts at 70°N may fall anywhere in the range 5–40 μm-atm from one orbit to the other. In the face of this variability the model results at 70°N (Figure 5) can be considered to be in good quantitative agreement with the observations: model O_3 values are in the range 10–35 μm-atm in the L_s = 330°–360° period. *Barth* [1985] attributed the large O_3 variability to rapid variations in the H_2O content. As discussed previously, we argue that the day-to-day variability observed by Mariner 9 was essentially of dynamical origin. Our results show that dynamical disturbances of the polar vortex may lead to large excursions in latitude of the polar vortex edge, characterized by strong O_3 gradients. Three-dimensional model simulations run at higher horizontal resolution would resolve better small-scale structures in the O_3 field at this time of the year. This would certainly increase further the O_3 variability that we find at 70°N (±10 μm-atm in 24 hours) and would be in even better agreement with the Mariner 9 data. Equatorward of 40°N, Mariner 9 did not observe ozone at any time at L_s = 330°–360°. This is consistent with our simulation, which shows that the detection limit contour (3 μm-atm) lies at about 40°N in zonal average (Figure 1). Previous 2-D model results by *Moreau et al.* [1991] indicated O_3 amounts

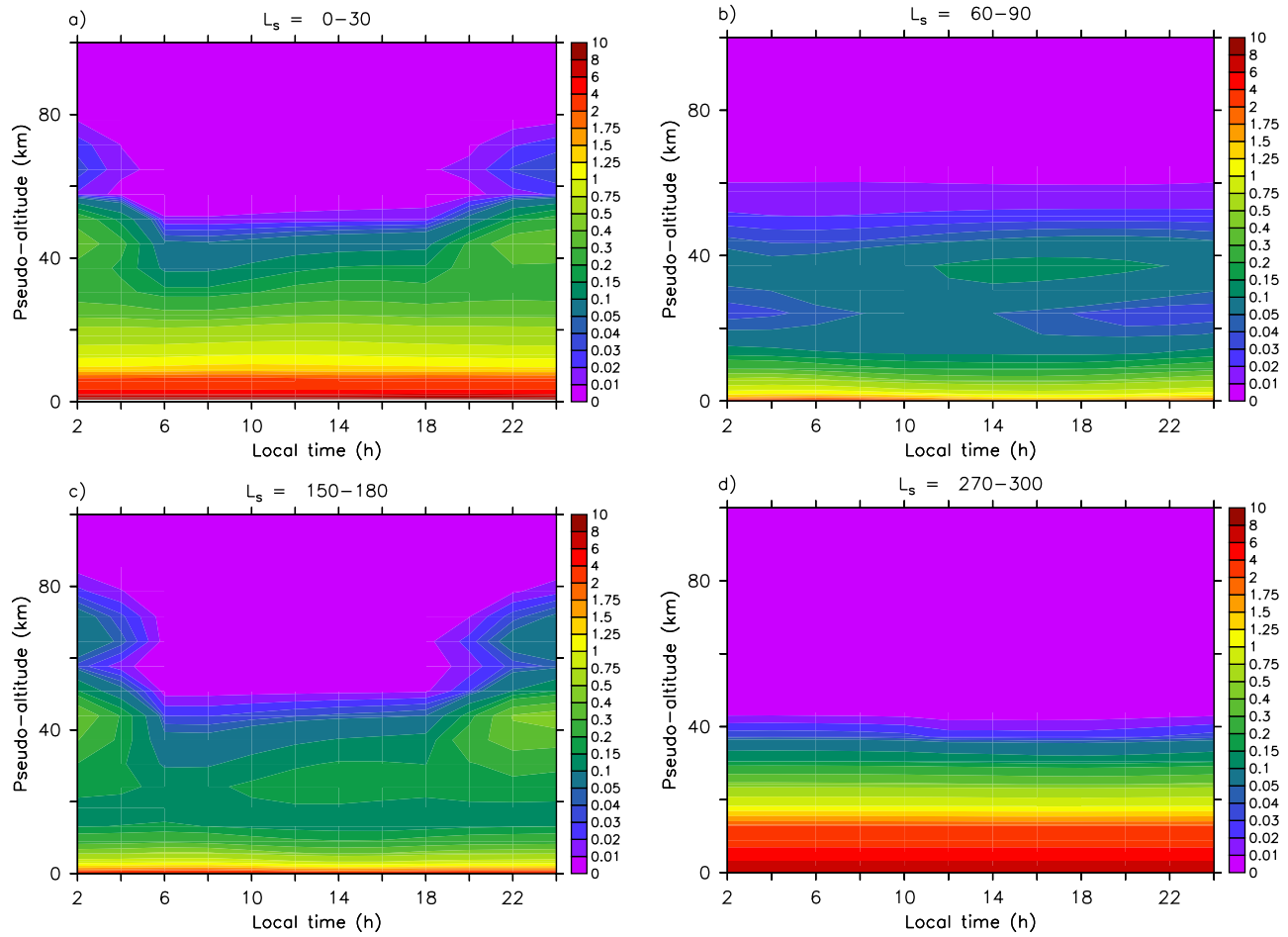

Figure 8. Diurnal variation of the vertical profile of ozone density ($\times 10^{10}$ cm^{-3}), at 70°N and longitude = 0°, averaged over four different seasons: (a) L_s = 0°–30°, (b) L_s = 60°–90°, (c) L_s = 150°–180°, and (d) L_s = 270°–300°.

of about 8 μm-atm at 40°N and 5 μm-atm at 20°N (L_s = 351°), which seem to be too large relative to the observations.

3.5.2. NH Spring/SH Fall (L_s = 0°–90°)

[43] *Clancy et al.* [1999] employed the Faint Object Spectrograph (FOS) on the HST to measure the latitudinal distribution of ozone in NH spring at L_s = 10° (September 1996) and L_s = 61° (January 1997). The model results are compared to these observations in Figure 9. For both periods the O_3 column daytime value was extracted from the model at the same L_s for five different longitudes spanning the quadrant of the Martian globe where the measurements were performed. At L_s = 10°, shortly after northern spring equinox, the model ozone columns are in excellent agreement with the observed values. As already shown in Figure 3, the effects of topography are important at this season. The five curves in Figure 9 are taken at longitudes with different surface elevation and explain much of the variability of the measurements, as already speculated by *Clancy et al.* [1999]. The strong latitudinal gradient of high-latitude O_3 is also well reproduced by the model, both in intensity and in geographical position.

[44] Mariner 9 data are available in NH midspring at $L_s \simeq$ 45°. Only the maximum O_3 amounts detected in the 50°N–75°N latitude band were shown by *Barth et al.* [1973], with values in the 5–17 μm-atm range. Considering the O_3 latitudinal gradient and longitudinal variability that exist in this season, these observations do not seem to contradict the model results (Figure 1). In the absence of more accurate information about the exact location of the measurements it is difficult, however, to go further in the analysis.

[45] Later in the NH spring season, at L_s = 61°, the comparison of our results with the FOS data does not show an agreement as good as at L_s = 10° (Figure 9b). Although the calculated seasonal decrease in the high-latitude O_3 seems consistent with the observations, there is about 50% less ozone at low latitudes to midlatitudes than measured by *Clancy et al.* [1999]. At latitudes south of 20°N, note that the model does produce increased O_3 columns compared to what is obtained at L_s = 10°. However, the amplitude of this seasonal variation is largely underestimated. Let us reiterate that the H_2O total column does not show a marked trend during this period. According to our model, the increase in O_3 column is essentially driven by the growth of the "aphelion layer" above 25 km, which results from the decrease in the hygropause altitude. Considering the good agreement obtained at L_s = 10°, when the surface O_3 layer is the dominant contributor to the total column, the underestimation of O_3 at L_s = 61° might indicate that the increase in the O_3 middle atmosphere layer is not strong enough.

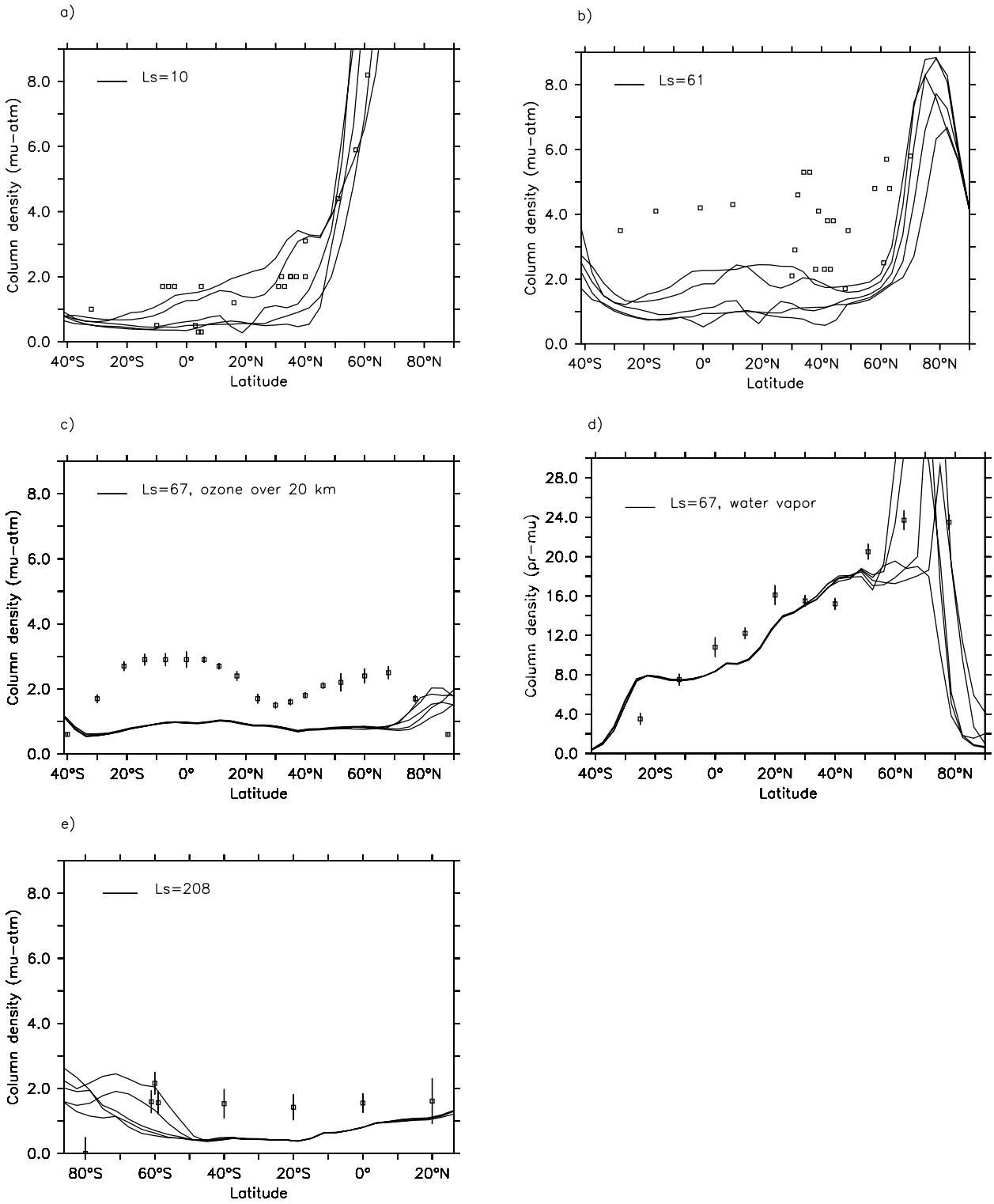

Figure 9. Comparison of model results with available observations. (a) O_3 column (μm-atm) at L_s = 10°. Solid lines: five model longitudes in the 90°W–180°W sector, local time is noon at 90°W. Squares: measurements by *Clancy et al.* [1999]. (b) Same at L_s = 61°. (c) O_3 column (μm-atm) at L_s = 67°. Solid lines: five consecutive days of the model. O_3 column is vertically integrated above 20 km altitude. Longitude is 308°E; local time is 1430. Squares: measurements by *Novak et al.* [2002]. These O_3 columns derived from the $O_2(a^1\Delta_g)$ dayglow emission may be subject to a reduction factor of 1.95. See text and *Krasnopolsky* [2003c]. (d) H_2O column (precipitable μm) at L_s = 67°. Solid lines: five consecutive days of the model. Longitude is 325°E; local time is 1540. Squares: measurements by *Novak et al.* [2002]. (e) O_3 column (μm-atm) at L_s = 208°. Solid lines: five consecutive days of the model. Longitude is 180°E; local time is noon. Squares: measurements by *Espenak et al.* [1991].

[46] *Novak et al.* [2002] (Figure 9c) retrieved the ozone column above ~20 km from the $O_2(a^1\Delta_g)$ dayglow emission at the same season (L_s = 67°, January 1997) as *Clancy et al.* [1999]. When integrated over the same altitude range, the model O_3 columns at low latitudes to midlatitudes are smaller than the observational data. If we exclude the measured O_3 minimum around 25°N, which may be related to the presence of clouds reducing the signal [*Novak et al.*, 2002], we note that the O_3 underestimation by the model is quantitatively similar to what is obtained at L_s = 61° with *Clancy et al.* [1999] data. The fact that the measurements of the $O_2(a^1\Delta_g)$ dayglow emission are sensitive only to the O_3 located above ~20 km might indicate that most of the discrepancy between the model and the data lies in the O_3 middle atmosphere layer rather than in the O_3 surface layer. However, the middle atmosphere O_3 abundance is rather poorly defined by the $O_2(a^1\Delta_g)$ dayglow emission alone. The relationship between both quantities depends on relatively uncertain rate coefficients and also requires the shape of the O_3 vertical profile, which is unknown at the time of the measurement. Using different parameters, *Krasnopolsky* [2003c] suggested that the O_3 columns calculated by *Novak et al.* [2002] should be reduced by a factor of 1.95. This reduction factor would bring their observations in much better agreement with our model calculations. Thus comparisons of O_3 columns derived from $O_2(a^1\Delta_g)$ dayglow emission with model results must be considered with caution. The conversion of the ozone vertical profiles calculated in the model to dayglow intensities should provide less uncertain comparisons. They will be the subject of a forthcoming dedicated paper.

[47] The water vapor columns derived by *Novak et al.* [2002] at L_s = 67° are not subject to the same uncertainty as their derived O_3 columns. The comparison with the model H_2O columns shows good agreement (Figure 9d), in terms of both absolute amounts and latitudinal gradient. Therefore an overestimation of the total H_2O by the model cannot be invoked to explain the too low O_3 amounts at this time of the year. This does not exclude, however, an excess in the H_2O mixing ratio at elevated altitude levels. Above the hygropause level the H_2O number density is small and decreases very rapidly with altitude: a possible wet bias in the model would not be detectable when examining only the total H_2O column.

3.5.3. NH Summer/SH Winter (L_s = 90°–180°)

[48] The only published observational data of O_3 in NH summer are those collected at the end of the Mariner 9 mission near L_s = 102°. Ozone was searched above the north polar cap and was found to be below the 3 μm-atm detection limit of the instrument. The model indicates O_3 columns of the order of 1 μm-atm at these latitudes (Figures 1 and 3b) and is therefore consistent with this observation.

3.5.4. NH Fall/SH Spring (L_s = 180°–270°)

[49] Using infrared spectroscopy, *Espenak et al.* [1991] measured O_3 from 80°S to 20°N in SH spring at L_s = 208°. The retrieved O_3 columns were less than 2.2 μm-atm at all latitudes sampled (Figure 9e). When taking into account the day-to-day variability, the model results are consistent with the observations made at 20°N and 60°S. The only previous ozone measurement at this season ($L_s \simeq 204°$) was made above the south polar cap by Mariner 7 and revealed an O_3 abundance of about 10 μm-atm [*Barth and Hord*, 1971]. To explain the much smaller abundance retrieved at SH high latitudes, *Espenak et al.* [1991] invoked the possible role of heterogeneous chemistry in controlling ozone variability. The good agreement that we obtain at 60°S with a pure gas-phase scheme suggests that heterogeneous processes may not be necessary to explain this particular observation. At 80°S the upper limit of 0.5 μm-atm given by *Espenak et al.* [1991] shows an even greater difference with the Mariner 7 observations. The model results are in the range 1–2 μm-atm but evolve rapidly with time: the limit of 0.5 μm-atm at 80°S is reached shortly after the measurement at L_s = 220°. Near the pole, O_3 is rapidly decreasing at this season as a result of the release of water vapor from the receding south polar cap (Figure 1). Because the timing of this O_3 decline is rather sensitive to details of the GCM water and dust cycles, as well as horizontal resolution, we think that the discrepancy noted at 80°S must not be overinterpreted. More problematic is the underestimation of O_3 between 40°S and the equator. Compared to what is found near aphelion, the difference with the observations is, however, reduced (~1 μm), which might be related to the lesser role the O_3 middle atmosphere layer is expected to play at this season. Thus the underestimation of O_3 by the model noticed at L_s = 61° and L_s = 208° could have the same origin, but measurements of the O_3 vertical profile will be needed to clarify this issue. For both seasons we emphasize that the calculated H_2O column amounts are in rather good agreement with the observational data (see Figure 9d at L_s = 67° and *Smith* [2002] for L_s = 208°). We reject overestimation of the low-atmosphere H_2O as a cause of the low O_3 bias in the model.

3.6. Discussion

[50] The model reproduces successfully many features of the available measurements of ozone on Mars. In particular, the results obtained in the period corresponding to the northern hemisphere winter and early spring appear to be in good quantitative agreement with the observational data. An outstanding problem is the underestimation of O_3 that is computed in late spring, near aphelion. A possible cause might be the substantial uncertainty that is associated with some important photochemical and kinetics parameters of Martian interest. We now examine the model sensitivity to the choice of these parameters. The crude assumption of a constant dust loading in the photochemical routine is also checked.

3.6.1. CO_2 Absorption Cross Sections

[51] The CO_2 absorption cross sections have a critical impact on the Martian photochemistry. When photolyzed, CO_2 is the primary source of odd oxygen at all altitudes. It is also the main ultraviolet absorber of the atmosphere of Mars: the CO_2 absorption spectrum controls the transmitivity of the atmosphere and therefore also affects the photolysis rate of other species involved in the ozone chemistry, such as H_2O or O_2.

[52] Since the measurements of *DeMore and Patapoff* [1972], followed by those of *Lewis and Carver* [1983] and *Parkinson et al.* [2003], it has been known that the CO_2 absorption spectrum shows a significant sensitivity to temperature as well as large variations over small wavelength intervals. In the CO_2 absorption region our photolysis rate calculations are made at a spectral resolution that is a factor of 10 (from 124 to 175 nm) to 500 (from 175 to 205 nm)

larger than the resolution of 5 nm already considered to be adequate by *Anbar et al.* [1993a]. Therefore the possible problems associated with data averaging over large intervals can be excluded. The situation with the low-temperature data is less satisfactory. In particular, a potentially important problem concerns the value of the CO_2 absorption cross sections at temperatures lower than those at which laboratory data are available. In the reference experiment described in this paper, we assumed that the cross sections below 200 K were identical to the values measured at 200 K. However, as shown by *Anbar et al.* [1993a], the computed photodissociation rates are quite sensitive to the manner of estimating the temperature dependence below 200 K. In a second 3-D model experiment (hereafter called case A) we extrapolated the temperature dependence of the CO_2 cross sections measured between 300 K and 200 K to the temperatures below 200 K. This assumption leads to significantly lower CO_2 absorption and UV opacity, in particular in the middle atmosphere, where temperatures are typically in the 140–160 K range. Subsequently, between 30 and 50 km the case A values for J_{H_2O} are about 100% larger than those obtained in the reference experiment. This result, obtained at a 60° SZA, is in good agreement with *Anbar et al.* [1993a]. Less sensitivity is found at lower altitudes, where the temperatures approach or are above 200 K: compared to the reference case, J_{H_2O} in case A shows a 30% increase at 20 km and only a 10% increase at the ground level. In contrast, the case A values for J_{CO_2} are lower than the reference values by about 30% above 50 km. At these altitudes the effect of the decreased CO_2 cross sections dominates the effect of the reduced atmospheric opacity. The opposite effect is found in the lower atmosphere (0–20 km), where J_{CO_2} slightly increases (+5 to +15%) in case A. The O_3 latitudinal distribution obtained with case A at $L_s = 61°$ is compared to the reference experiment and the measurements by *Clancy et al.* [1999] in Figure 10. At all latitudes the O_3 columns of case A are smaller than those of the reference experiment. This was expected from the larger J_{H_2O}, which causes up to a doubling of the HO_x abundance at the hygropause level. As a result, the O_3 mixing ratio is reduced by half around 30 km altitude. Thus extrapolating the temperature dependence of the CO_2 cross sections below 200 K does not reduce the discrepancy between the model and the observational data. On the contrary, even smaller O_3 columns are computed with this assumption, which suggests that the solution to increase O_3 near aphelion must be found elsewhere.

3.6.2. H_2O Absorption Cross Sections

[53] The production of ozone-destroying HO_x radicals occurs through the photolysis of water vapor in the ultraviolet. H_2O absorption cross sections are now available to good accuracy up to 196 nm [*Cheng et al.*, 1999]. However, measurements were performed at room temperature (295 K), and there is no information regarding a possible temperature dependence in the long-wavelength tail, similar to that of the CO_2 absorption cross section. *Krasnopolsky* [1993] and *Atreya and Gu* [1994] reduced the H_2O absorption cross sections by a factor of 2 to investigate the effect of their possible temperature dependence and found a better agreement between the production and loss of CO_2. The reduction in the HO_x production that resulted from the smaller H_2O cross sections also led to an increase in the calculated O_3, found to be of the order of 15% by *Krasnopolsky* [1993]. On the other hand, *Nair et al.* [1994] noted that the extrapolation of the H_2O cross sections from 196 nm out to 210 nm, assuming a linear decrease with the logarithm of the cross section, leads to an opposite effect, with a 25% decrease in ozone. Model results are therefore relatively sensitive to the assumed H_2O absorption at temperatures and wavelengths for which laboratory data are not available. On the basis of the numbers mentioned above, it seems unlikely, however, that a better knowledge of the H_2O cross sections could lead to the doubling of the O_3 column that is needed to match the observations made near aphelion.

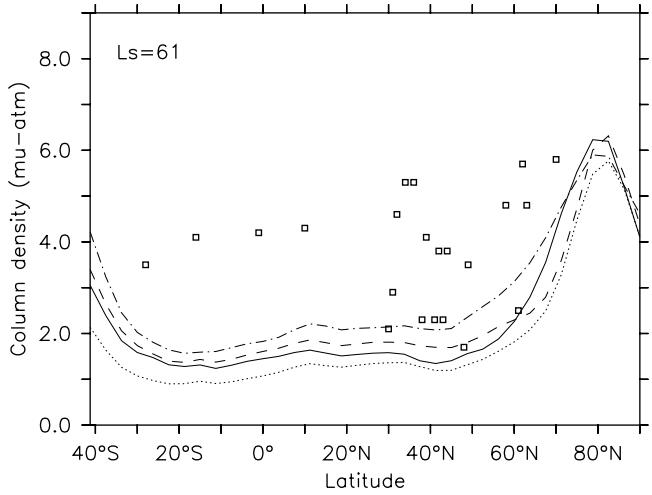

Figure 10. Comparison of model results with O_3 column observations (μm-atm) at $L_s = 61°$. Squares: measurements by *Clancy et al.* [1999]. Solid line: reference simulation. Dotted line: case A, extrapolation of the temperature dependence of CO_2 cross sections below 200 K. Dashed line: case B, revised HO_x kinetics, from the work of *Jucks et al.* [1998]. Dash-dotted line: case C, dust optical depth multiplied by 10 ($\tau_{dust} = 2$).

3.6.3. HO_x Reaction Rates

[54] In addition to the H_2O photolysis, the other main process controlling the abundance of HO_x radicals in the Martian atmosphere is the loss mechanism c_{07}:

$$OH + HO_2 \rightarrow H_2O + O_2$$

The rate of this reaction is still subject to a large uncertainty, which might directly affect the amount of calculated ozone in the model. In our reference simulation we used for c_{07} the value recommended by *Sander et al.* [2003], who estimate the uncertainty to be about 50% at 200 K. In order to reproduce better the observed abundances of CO, O_2, and O_3, *Nair et al.* [1994] proposed to increase the rate of c_{07} by 81%, a change also adopted by *Clancy and Nair* [1996]. However, this modification is inconsistent with the observations performed in the terrestrial stratosphere by *Jucks et al.* [1998], who provided the only set of simultaneous vertical profiles of OH and HO_2. According to their study, the measured OH and HO_2 are modeled best by calculations that use, on the contrary, a 25% decrease in

the c_{07} rate, together with a 25% decrease in the reaction rate of c_{01}:

$$HO_2 + O \rightarrow OH + O_2$$

We have tested the impact of these kinetics changes in a third simulation of the coupled model (hereafter called case B). The ozone column meridional distribution obtained with case B at $L_s = 61°$ is compared to the reference simulation and case A in Figure 10. At low latitudes to midlatitudes, a moderate (+5 to +25%) increase is found relative to the reference experiment, but the obtained values are still significantly smaller than the observations. Interestingly, the increased ozone column found in case B is obtained in an atmosphere that is richer in HO_x. This is explained by the reduced rate of reaction c_{01}, which is the main loss mechanism of odd oxygen in the lower atmosphere. This change outweighs the effect of the increase in HO_x that results from the reduced efficiency of reaction c_{07}. However, the overall effect on the O_3 column remains limited. The kinetics parameters required to explain the observations of OH and HO_2 on Earth do not appear to be the solution to reaching a satisfying quantitative agreement between the model and the measurements in the Mars aphelion season.

3.6.4. Dust and Clouds

[55] Another possibility is that the assumed dust loading in the model differs significantly from the actual dust levels on Mars when the O_3 observations were made in January 1997. In his comprehensive modeling study of the effect of airborne particles on ozone on Mars, *Lindner* [1988] showed that O_3 increases when dust opacity increases. This arises because the absorption of solar radiation by dust reduces more effectively the O_3 loss mechanisms (H_2O photolysis and odd hydrogen catalytic cycles) than the O_3 production mechanism (CO_2 photolysis and reaction a_{01}). Too low O_3 amounts could then result from the underestimation of dust opacity in the model. This hypothesis is not supported by the observations. On the contrary, *Clancy et al.* [1999] reported minimal dust loading in January 1997 ($\tau_{dust} \leq 0.2$), meaning that our assumed dust optical depth ($\tau_{dust} = 0.2$) is actually an upper limit. Thus we rule out the underestimation of dust as a possible explanation for the too low O_3 amounts computed near aphelion. This conclusion is reinforced by the sensitivity experiment (case C) carried out with an extreme level of dust ($\tau_{dust} = 2.0$) similar to those reported during global dust storms [*Zurek*, 1982]. Even with this unrealistically large dust loading for 1997, it can be seen in Figure 10 that the modeled O_3 increase at low latitudes to midlatitudes (+15 to +40%) is still largely insufficient to match the observations.

[56] Unlike dust, the effect of water ice clouds on photolysis rates is not implemented in the model. However, as shown by *Lindner* [1988], scattering of the incoming solar radiation by clouds does little to change the O_3 abundance. Using a cloud opacity of $\tau_{cloud} = 0.5$ at 57°N, *Lindner* [1988] found slightly less ozone than in a cloudless case, with a maximum reduction of only ~5% at 40 km. Note that water ice cloud opacities reported in the aphelion equatorial belt are more generally in the range $\tau_{cloud} = 0.2–0.3$ [*James et al.*, 1994; *Wolff et al.*, 1999] and were as low as 0.02–0.08 in 1997 [*Clancy et al.*, 1999]. Furthermore, because of smaller SZAs, photolysis rates are expected to be less affected by clouds at low latitudes to midlatitudes than at 57°N. For both reasons the impact of the aphelion cloud belt on photolysis rates and O_3 should be even weaker than in the case discussed by *Lindner* [1988] and hence may be safely neglected.

[57] In addition to the absorption and scattering of the incoming solar radiation, airborne particles can also provide appropriate adsorption sites for heterogeneous chemical reactions to occur. This issue has often been a matter of debate in past 1-D modeling studies. *Anbar et al.* [1993b] demonstrated that heterogeneous chemistry could be important in lowering the abundance of HO_x in the Martian atmosphere but also emphasized the clear need for laboratory data to constrain better the rate of HO_x adsorption on surfaces and at temperatures more representative of Mars. The large uncertainties that affect critical parameters such as the HO_x reaction probabilities on dust and ice, or the altitude distribution of aerosols, are perhaps at the origin of the contradictory results found in the literature. Several studies noted a better agreement with the observations when a heterogeneous sink of HO_x is taken into account [*Krasnopolsky*, 1993, 2003b; *Atreya and Gu*, 1994], while others concluded that there was no need to invoke such processes to reconcile models and observations [*Nair et al.*, 1994; *Clancy et al.*, 2004]. It must also be realized that the inclusion of heterogeneous chemistry in 1-D models can only provide first-order results, which represent globally and seasonally averaged conditions. The fact that a 3-D homogeneous gas-phase model is unable to reproduce O_3 amounts observed at specific times and locations is a much stronger indication that some heterogeneous process may be needed. This argument is reinforced by the manipulations of gas-phase data previously discussed, of which none seems to be a viable option to solve the model difficulties. Thus, because the adsorption of HO_x is expected to increase the O_3 amount, heterogeneous chemistry is a particularly attractive candidate in the aphelion season. However, if it is the only important missing process, it must not degrade in the same time the satisfactory results obtained with the gas-phase homogeneous scheme in the postperihelion period. In terms of aerosols this may suggest that heterogeneous processes must be especially effective on water ice clouds, which are known to dominate at the largest Sun-Mars distances, rather than on dust, which is much more abundant in the perihelion period [*Clancy et al.*, 2003]. This first-order indication will have to be confirmed by a dedicated study that will be the subject of another paper.

4. Conclusion

[58] The model simulations presented here establish an updated picture of our understanding of the ozone chemistry and transport on Mars. The results do not contradict the fundamental aspects of the ozone behavior that were previously predicted by 1-D and 2-D modeling studies. However, the coupling between the photochemistry, a consistent representation of the Martian water cycle, and three-dimensional transport make it possible to go further in the analysis of the O_3 variability on various scales of time and space.

[59] We find that the classical anticorrelation expected between the O_3 and H_2O columns is spatially verified only

at a given solar longitude. Over the Martian year the low-latitude O_3 column shows, for instance, little anticorrelation with the H_2O column. At high latitudes, O_3 may even look correlated with H_2O if one compares the columns of each hemisphere in summer.

[60] Departures from the expected anticorrelation between the O_3 and H_2O columns are almost entirely due to orbital (L_s) variations in the H_2O vertical distribution. Our results confirm the effectiveness of a mechanism first hypothesized by *Clancy and Nair* [1996]: over the period $L_s = 180°–330°$ centered on perihelion, water vapor saturation occurs in the model at high altitude (>40 km at $L_s = 250°$), leading to considerable HO_x production and O_x loss in the middle atmosphere. As a result, O_3 is essentially confined in a "surface layer" below 20 km. During the rest of the year ($L_s = 330°–180°$), the altitude of water vapor saturation is lower (~10 km at $L_s = 90°$), which reduces the HO_x production and allows the formation of an additional O_3 layer at 25–70 km. The maximum O_3 densities in this layer are reached around aphelion.

[61] In general, less ozone is computed during the day than during the night. The daytime low-latitude to midlatitude O_3 column is maximum in midmorning, whereas little change is observed over the night. The amplitude of this diurnal cycle is linked to the presence of the O_3 middle atmosphere layer, which is characterized by daytime densities about one order of magnitude smaller than during the night. Near perihelion, the absence of this layer leads to the complete disappearance of the day-night contrast in the total ozone field.

[62] Other aspects of the ozone variability on Mars are more specifically three-dimensional and are represented for the first time. Topography is the main factor modulating the O_3 column in the perihelion season and explains the variability of the measurements made at this time of the year. At high latitudes, dynamics and horizontal transport play an important role when the O_3 photochemical lifetime becomes long in winter and early spring. The model reproduces rather well the wide day-to-day O_3 variations observed by Mariner 9, which are shown to be related to dynamical disturbances of the polar vortex.

[63] The stringent comparison of the modeled Mars O_3 abundance with observational data reveals contrasted results. A good quantitative agreement is found in the postperihelion period ($L_s = 290°–10°$), but the model fails to reproduce O_3 columns as large as those measured near aphelion ($L_s = 61°–67°$). Current uncertainties in absorption cross sections and gas-phase kinetics data do not seem to provide credible explanations to explain this discrepancy. This supports the possible existence of heterogeneous processes removing odd hydrogen radicals, as suggested by previous 1-D model studies [*Krasnopolsky*, 1993, 2003b; *Atreya and Gu*, 1994]. However, the probabilities of these reactions on the surfaces of Martian interest are still poorly documented by laboratory data, especially at low temperatures. Their potential impact on the ozone abundance in our model will require a dedicated study.

[64] Although the total water vapor columns computed by the model generally agree with the observations, we do not exclude a possible overestimation of the high-altitude H_2O mixing ratio as a possible cause for the too low O_3 amounts in the aphelion season. Clearly, systematic measurements of the ozone and water vapor vertical profiles would be highly desirable to clarify this issue. Recently arrived at Mars, the SPICAM UV and infrared spectrometer [*Bertaux et al.*, 2000] on board Mars Express should provide an unprecedented wealth of simultaneous observations of ozone and water vapor. These new data sets will improve significantly our knowledge of the three-dimensional distribution of ozone on Mars and provide the chemical models with the strongest observational constraints to date. As they do for the terrestrial atmosphere, it is likely that three-dimensional chemical models will play a major role in their interpretation and will be invaluable tools to make further progress toward a quantitative understanding of the Martian photochemistry.

[65] **Acknowledgments.** We are grateful to Vladimir Krasnopolsky and Robert Novak for their manuscript reviews. S.L. acknowledges support from the postdoctoral fellowship program of Centre National d'Etudes Spatiales (CNES). F.M. is supported by a National Research Council Research Associateship Award at NASA Ames Research Center.

References

Anbar, A. D., M. Allen, and H. A. Nair (1993a), Photodissociation in the atmosphere of Mars: Impact of high-resolution temperature-dependent CO_2 cross-section measurements, *J. Geophys. Res.*, *98*(E6), 10,925–10,931.

Anbar, A. D., M.-T. Leu, H. A. Nair, and Y. L. Yung (1993b), Adsorption of HO_x on aerosol surfaces: Implications for the atmosphere of Mars, *J. Geophys. Res.*, *98*(E6), 10,933–10,940.

Angelats-i-Coll, M., F. Forget, M. A. Lopez-Valverde, P. L. Read, and S. R. Lewis (2004), Upper atmosphere of Mars up to 120 km: Mars Global Surveyor accelerometer data analysis with the LMD general circulation model, *J. Geophys. Res.*, *109*(E1), E01011, doi:10.1029/2003JE002163.

Atreya, S. K., and Z. G. Gu (1994), Stability of the Martian atmosphere: Is heterogeneous catalysis essential?, *J. Geophys. Res.*, *99*(E6), 13,133–13,145.

Barth, C. A. (1985), The photochemistry of the atmosphere of Mars, pp. 337–392, Academic, San Diego, Calif.

Barth, C. A., and C. W. Hord (1971), Mariner ultraviolet spectrometer: Topography and polar cap, *Science*, *173*(3993), 197–201.

Barth, C. A., C. W. Hord, A. I. Stewart, A. L. Lane, M. L. Duck, and G. P. Anderson (1973), Mariner 9 ultraviolet spectrometer experiment: Seasonal variation of ozone on Mars, *Science*, *179*, 795–796.

Baulch, D. L., et al. (1992), Evaluated kinetic data for combustion modeling, *J. Phys. Chem. Ref. Data*, *21*(3), 411–734.

Bertaux, J.-L., et al. (2000), The study of the Martian atmosphere from top to bottom with SPICAM light on Mars Express, *Planet. Space Sci.*, *48*, 1303–1320.

Blamont, J. E., and E. Chassefière (1993), First detection of ozone in the middle atmosphere of Mars from solar occultation measurements, *Icarus*, *104*, 324–336.

Brasseur, G. P., and S. Solomon (1986), *Aeronomy of the Middle Atmosphere*, 2nd ed., 452 pp., D. Reidel, Norwell, Mass.

Chassefière, E., P. Drossart, and O. Korablev (1995), Post-Phobos model for the altitude and size distribution of dust in the low Martian atmosphere, *J. Geophys. Res.*, *100*, 5525–5540.

Cheng, B.-M., E. P. Chew, C. P. Liu, M. Bahou, Y.-P. Lee, Y. L. Yung, and M. F. Gerstell (1999), Photo-induced fractionation of water isotopomers in the Martian atmosphere, *Geophys. Res. Lett.*, *26*(24), 3657–3660.

Christensen, L. E., M. Okumora, S. P. Sander, R. J. Salawitch, G. C. Toon, B. Sen, J.-F. Blavier, and K. W. Jucks (2002), Kinetics of $HO_2 + HO_2 \rightarrow H_2O_2 + O_2$: Implications for stratospheric H_2O_2, *Geophys. Res. Lett.*, *29*(9), 1299, doi:10.1029/2001GL014525.

Clancy, R. T., and H. Nair (1996), Annual (perihelion-aphelion) cycles in the photochemical behavior of the global Mars atmosphere, *J. Geophys. Res.*, *101*(E5), 12,785–12,790.

Clancy, R. T., M. J. Wolff, P. B. James, E. Smith, Y. N. Billawala, S. W. Lee, and M. M. Callan (1996), Mars ozone measurements near the 1995 aphelion: Hubble Space Telescope ultraviolet spectroscopy with the Faint Object Spectrograph, *J. Geophys. Res.*, *101*(E5), 12,777–12,783.

Clancy, R. T., M. J. Wolff, and P. B. James (1999), Minimal aerosol loading and global increases in atmospheric ozone during the 1996–1997 Martian northern spring season, *Icarus*, *138*, 49–63.

Clancy, R. T., M. J. Wolff, and P. R. Christensen (2003), Mars aerosol studies with the MGS TES emission phase function observations: Optical

depths, particle sizes, and ice cloud types versus latitude and solar longitude, *J. Geophys. Res.*, *108*(E9), 5098, doi:10.1029/2003JE002058.
Clancy, R. T., B. J. Sandor, and G. H. Moriarty-Schieven (2004), A measurement of the 362 GHz absorption line of Mars atmospheric H_2O_2, *Icarus*, *168*, 116–121.
DeMore, W. B., and M. Patapoff (1972), Temperature and pressure dependence of CO_2 extinction coefficients, *J. Geophys. Res.*, *77*, 6291–6293.
Encrenaz, T., B. Bézard, T. K. Greathouse, M. J. Richter, J. H. Lacy, S. K. Atreya, A. S. Wong, S. Lebonnois, F. Lefèvre, and F. Forget (2004), Hydrogen peroxide on Mars: Evidence for spatial and seasonal variations, *Icarus*, in press.
Espenak, F., M. J. Mumma, T. Kostiuk, and D. Zipoy (1991), Ground-based infrared measurements of the global distribution of ozone in the atmosphere of Mars, *Icarus*, *92*, 252–262.
Forget, F., F. Hourdin, R. Fournier, C. Hourdin, O. Talagrand, M. Collins, S. R. Lewis, P. L. Read, and J.-P. Huot (1999), Improved general circulation models of the Martian atmosphere from the surface to above 80 km, *J. Geophys. Res.*, *104*(E10), 24,155–24,176.
Forget, F., Y. Wanherdrick, and S. R. Lewis (2001), Validation of the Mars general circulation model and climate database with new spacecraft observations, *Tech. Note 11369/95/NL/JG*, Eur. Space Agency, Paris.
Hinson, D. P., M. Flasar, R. A. Simpson, J. D. Twicken, and G. L. Tyler (1999), Initial results from radio occultation measurements with Mars Global Surveyor, *J. Geophys. Res.*, *104*(E11), 26,997–27,012.
Hourdin, F., and A. Armengaud (1999), Test of a hierarchy of finite-volume schemes for transport of trace species in an atmospheric general circulation model, *Mon. Weather Rev.*, *127*, 822–837.
Jakosky, B. M., and C. B. Farmer (1982), The seasonal and global behavior of water vapor in the Mars atmosphere: Complete global results of the Viking atmospheric water detector experiment, *J. Geophys. Res.*, *87*, 2999–3019.
James, P. B., R. T. Clancy, S. W. Lee, L. J. Martin, R. B. Singer, E. Smith, R. A. Kahn, and R. W. Zurek (1994), Monitoring Mars with the Hubble Space Telescope: 1990–1991 observations, *Icarus*, *109*, 79–101.
Jucks, K. W., D. G. Johnson, K. V. Chance, W. A. Traub, J. J. Margitan, G. B. Osterman, R. J. Salawitch, and Y. Sasano (1998), Observations of OH, HO_2, H_2O and O_3 in the upper stratosphere: Implications for HO_x photochemistry, *Geophys. Res. Lett.*, *25*, 3935–3938.
Krasnopolsky, V. A. (1993), Photochemistry of the Martian atmosphere (mean conditions), *Icarus*, *101*, 313–332.
Krasnopolsky, V. A. (2003a), Spectroscopic mapping of Mars CO mixing ratio: Detection of north-south asymmetry, *J. Geophys. Res.*, *108*(E2), 5010, doi:10.1029/2002JE001926.
Krasnopolsky, V. A. (2003b), Mars photochemistry: Weak points and search for solutions, paper presented at 6th International Conference on Mars, Lunar and Planet. Inst., Pasadena, Calif., 20–25 July .
Krasnopolsky, V. A. (2003c), Mapping of Mars O_2 1.27 μm dayglow at four seasonal points, *Icarus*, *165*, 315–325.
Krasnopolsky, V. A., and P. D. Feldman (2001), Detection of molecular hydrogen in the atmosphere of Mars, *Science*, *294*, 1914–1917.
Krasnopolsky, V. A., and V. A. Parshev (1979), Ozone photochemistry of the Martian lower atmosphere, *Planet. Space Sci.*, *27*, 113–120.
Krastitsky, O. P. (1978), A model for the diurnal variation of the composition of the Martian atmosphere, *Cosmic Res.*, Engl. Transl., *16*, 350–356.
Lefèvre, F., G. Brasseur, I. Folkins, A. K. Smith, and P. Simon (1994), Chemistry of the 1991–1992 stratospheric winter: Three-dimensional model simulations, *J. Geophys. Res.*, *99*, 8183–8195.
Lefèvre, F., F. Figarol, K. S. Carslaw, and T. Peter (1998), The 1997 Arctic ozone depletion quantified from three-dimensional simulations, *Geophys. Res. Lett.*, *25*, 2425–2428.
Lellouch, E., G. Paubert, and T. Encrenaz (1991), Mapping of CO millimeter-wave lines in Mars' atmosphere: The spatial distribution of carbon monoxide on Mars, *Planet. Space Sci.*, *39*, 219–224.
Lewis, J. S., and J. H. Carver (1983), Temperature dependence of the carbon dioxide photoabsorption cross section between 1200 and 170 Angstroms, *J. Quant. Spectrosc. Radiat. Transfer*, *30*, 297–309.
Lindner, B. L. (1988), Ozone on Mars: The effects of clouds and airborne dust, *Planet. Space Sci.*, *36*(2), 125–144.
Madronich, S., and S. Flocke (1998), *The Role of Solar Radiation in Atmospheric Chemistry*, pp. 1–26, Springer-Verlag, New York.
McCabe, D. C., T. Gierczak, R. K. Talukdar, and A. R. Ravishankara (2001), Kinetics of the reaction OH + CO under atmospheric conditions, *Geophys. Res. Lett.*, *28*, 3135–3138.
McElroy, M. B., and T. M. Donahue (1972), Stability of the Martian atmosphere, *Science*, *177*, 986–988.
Minschwaner, K., G. P. Anderson, L. A. Hall, and K. Yoshino (1992), Polynomial coefficients for calculating O_2 Schumann-Runge cross sections at 0.5 cm^{-1} resolution, *J. Geophys. Res.*, *97*, 10,103–10,108.
Molina, L. T., and M. J. Molina (1986), Absolute absorption cross sections of ozone in the 185- to 350-nm wavelength range, *J. Geophys. Res.*, *91*, 14,501–14,508.
Moreau, D., L. W. Esposito, and G. Brasseur (1991), The chemical composition of the dust-free Martian atmosphere: Preliminary results of a two-dimensional model, *J. Geophys. Res.*, *96*(B5), 7933–7945.
Nair, H., M. Allen, A. D. Anbar, Y. L. Yung, and R. T. Clancy (1994), A photochemical model of the Martian atmosphere, *Icarus*, *111*, 124–150.
Neckel, H., and D. Labs (1984), The solar radiation between 3300 and 12500 Å, *Sol. Phys.*, *90*, 205–258.
Novak, R. E., M. J. Mumma, M. A. DiSanti, N. Dello Russo, and K. Magee-Sauer (2002), Mapping of ozone and water in the atmosphere of Mars near the 1997 aphelion, *Icarus*, *158*, 14–23.
Novak, R. E., M. J. Mumma, M. A. DiSanti, N. Dello Russo, K. Magee-Sauer, and B. Bonev (2003), Seasonal and diurnal mapping of ozone and water in the Martian atmosphere, paper presented at 6th International Conference on Mars, Lunar and Planet. Inst., Pasadena, Calif., 20–25 July .
Owen, T., K. Biemann, D. R. Rushneck, J. E. Biller, D. W. Howarth, and A. L. Lafleur (1997), The composition of the atmosphere at the surface of Mars, *J. Geophys. Res.*, *82*, 4635–4639.
Pang, K., and J. M. Ajello (1977), Complex refractive index of Martian dust: Wavelength dependence and composition, *Icarus*, *30*, 63–74.
Parkinson, T. D., and D. M. Hunten (1972), Spectroscopy and aeronomy of O_2 on Mars, *J. Atmos. Sci.*, *29*, 1380–1390.
Parkinson, W. H., J. Rufus, and K. Yoshino (2003), Absolute cross section measurements of CO_2 in the wavelength region 163–200 nm and the temperature dependence, *Chem. Phys.*, *219*(1), 45–57.
Richardson, M. I., and R. J. Wilson (2002), Investigation of the nature and stability of the Martian seasonal water cycle with a general circulation model, *J. Geophys. Res.*, *107*(E5), 5031, doi:10.1029/2001JE001536.
Sander, S. P., et al (2003), *Chemical kinetics and photochemical data for use in atmospheric studies, Evaluation number 14, JPL Publ. 02-25*, Jet Propul. Lab., Pasadena, Calif.
Schuergers, M., and K. H. Welge (1968), Absorptionskoeffizient von H_2O_2 und N_2H_4 zwischen 1200 und 2000 Å, *Z. Naturforsch. A*, *23*, 1508–1510.
Shemansky, D. E. (1972), CO_2 extinction coefficient 1700–3000 A, *J. Chem. Phys.*, *56*, 1582–1587.
Shimazaki, T. (1981), A model of temporal variations in ozone density in the Martian atmosphere, *Planet. Space Sci.*, *29*, 21–33.
Shimazaki, T. (1985), *Minor Constituents in the Middle Atmosphere*, Terra Sci., Tokyo.
Smith, D. E., et al. (1999), The global topography of Mars and implications for surface evolution, *Science*, *284*, 1495–1503.
Smith, M. D. (2002), The annual cycle of water vapor on Mars as observed by the Thermal Emission Spectrometer, *J. Geophys. Res.*, *107*(E11), 5115, doi:10.1029/2001JE001522.
Smith, M. D., J. C. Pearl, B. J. Conrath, and P. R. Christensen (2001), Thermal Emission Spectrometer results: Mars atmospheric thermal structure and aerosol distribution, *J. Geophys. Res.*, *106*(E10), 23,929–23,945.
Stamnes, K., S.-C. Tsay, W. Wiscombe, and K. Jayaweera (1988), Numerically stable algorithm for discrete-ordinate-method radiative transfer in multiple scattering and emitting layered media, *Appl. Opt.*, *27*, 2502–2509.
Thompson, B. A., P. Harteck, and R. R. Reeves (1963), Ultraviolet absorption coefficients of CO_2, CO, O_2, H_2O, N_2O, NH_3, NO, SO_2, and CH_4 between 1850 and 4000 Å, *J. Geophys. Res.*, *68*, 6431–6436.
Traub, W. A., N. P. Carleton, P. Connes, and J. F. Noxon (1979), The latitude variation of O_2 dayglow and O_3 abundance on Mars, *Astrophys. J.*, *229*, 846–850.
Tsang, W., and R. F. Hampson (1986), Chemical kinetic data base for combustion chemistry. Part I. Methane and related compounds, *J. Phys. Chem. Ref. Data*, *15*, 1087–1279.
VanHoosier, M. E., J.-D. F. Bartoe, G. E. Bruekner, and D. K. Prinz (1988), Absolute solar spectral irradiance 120 nm–400 nm (results from Spacelab 2), *Astrophys. Lett. Commun.*, *27*, 163–168.
Van Leer, B. (1977), Towards the ultimate conservative difference scheme: IV. A new approach to numerical convection, *J. Comput. Phys.*, *23*, 276–299.
Wherbein, W. M., C. W. Hord, and C. A. Barth (1979), Mariner 9 ultraviolet spectrometer experiment: Vertical distribution of ozone on Mars, *Icarus*, *38*, 288–299.
Wolff, M. J., J. F. Bell III, P. B. James, R. T. Clancy, and S. W. Lee (1999), Hubble Space Telescope observations of the Martian aphelion cloud belt prior to the Pathfinder mission: Seasonal and interannual variations, *J. Geophys. Res.*, *104*, 9027–9041.

World Meteorological Organization (WMO) (1986), *Atmospheric Ozone: 1985*, WMO Rep. 16, Geneva.

Yoshino, K., A. S.-C. Cheung, J. R. Esmond, W. H. Parkinson, D. E. Freeman, S. L. Guberman, A. Jenouvrier, B. Coquart, and M. F. Merienne (1988), Improved absorption cross-sections of oxygen in the wavelength region 205–240 nm of the Herzberg continuum, *Planet. Space Sci.*, *36*, 1469–1475.

Yoshino, K., J. R. Esmond, Y. Sun, W. H. Parkinson, K. Ito, and T. Matsui (1996a), Absorption cross section measurements of carbon dioxide in the wavelength region 118.7–175.5 and the temperature dependence, *J. Quant. Spectrosc. Radiat. Transfer*, *55*, 53–60.

Yoshino, K., J. R. Esmond, W. H. Parkinson, K. Ito, and T. Matsui (1996b), Absorption cross section measurements of water vapor in the wavelength region 120 to 188 nm, *Chem. Phys.*, *211*, 387–391.

Zurek, R. W. (1982), Martian great dust storms: An update, *Icarus*, *50*, 288–310.

F. Forget and S. Lebonnois, Laboratoire de Météorologie Dynamique, Institut Pierre-Simon Laplace, 4 place Jussieu, Box 99, F-75252 Paris Cedex 05, France. (francois.forget@lmd.jussieu.fr; sebastien.lebonnois@lmd.jussieu.fr)

F. Lefèvre, Service d'Aéronomie, Institut Pierre-Simon Laplace, 4 place Jussieu, Box 102, F-75252 Paris Cedex 05, France. (franck.lefevre@aero.jussieu.fr)

F. Montmessin, Space Science Division, NASA Ames Research Center, MS 245-3, Moffett Field, CA 94035-1000, USA. (fmontmessin@mail.arc.nasa.gov)